

## rf breakdown measurements in electron beam driven 200 GHz copper and copper-silver accelerating structures

Massimo Dal Forno,<sup>1,\*</sup> Valery Dolgashev,<sup>1</sup> Gordon Bowden,<sup>1</sup> Christine Clarke,<sup>1</sup>  
Mark Hogan,<sup>1</sup> Doug McCormick,<sup>1</sup> Alexander Novokhatski,<sup>1</sup> Brendan O'Shea,<sup>1</sup>  
Bruno Spataro,<sup>2</sup> Stephen Weathersby,<sup>1</sup> and Sami G. Tantawi<sup>1</sup>

<sup>1</sup>SLAC National Accelerator Laboratory, Menlo Park, California 94025, USA

<sup>2</sup>INFN/LNF Frascati, Via E. Fermi, 40, Frascati (Roma) 00044, Italy

(Received 30 July 2016; published 30 November 2016)

This paper explores the physics of vacuum rf breakdowns in subterahertz high-gradient traveling-wave accelerating structures. We present the experimental results of rf tests of 200 GHz metallic accelerating structures, made of copper and copper-silver. These experiments were carried out at the Facility for Advanced Accelerator Experimental Tests (FACET) at the SLAC National Accelerator Laboratory. The rf fields were excited by the FACET ultrarelativistic electron beam. The traveling-wave structure is an open geometry, 10 cm long, composed of two halves separated by a gap. The rf frequency of the fundamental accelerating mode depends on the gap size and can be changed from 160 to 235 GHz. When the beam travels off axis, a deflecting field is induced in addition to the longitudinal field. We measure the deflecting forces by observing the displacement of the electron bunch and use this measurement to verify the expected accelerating gradient. Furthermore, we present the first quantitative measurement of rf breakdown rates in 200 GHz metallic accelerating structures. The breakdown rate of the copper structure is  $10^{-2}$  per pulse, with a peak surface electric field of 500 MV/m and a rf pulse length of 0.3 ns, which at a relatively large gap of 1.5 mm, or one wavelength, corresponds to an accelerating gradient of 56 MV/m. For the same breakdown rate, the copper-silver structure has a peak electric field of 320 MV/m at a pulse length of 0.5 ns. For a gap of 1.1 mm, or 0.74 wavelengths, this corresponds to an accelerating gradient of 50 MV/m.

DOI: 10.1103/PhysRevAccelBeams.19.111301

### I. INTRODUCTION

The accelerating gradient is one of the crucial parameters affecting the design, construction, and cost of the next-generation linear accelerators. The challenge is to develop reliable and cost-effective high-gradient accelerators.

The typical working frequencies of linear accelerators are from about 1 to 12 GHz. The accelerating gradient of the long-lived SLAC S-band linac is about 17 MV/m [1]. During development of the Next Linear Collider (NLC)/Global Linear Collider (GLC), an X-band test accelerator operated at 65 MV/m unloaded gradient [2,3]. The CERN-based linear collider design Compact Linear Collider (CLIC) requires 100 MV/m loaded gradient at 12 GHz in accelerating structures with heavy wakefield damping [4]. Future accelerators such as compact synchrotron light sources or inverse Compton scattering gamma-ray sources [5] may need even higher gradients.

High-gradient acceleration has several problems: rf breakdown, pulsed surface heating, and field emission are the major obstacles [6]. rf breakdowns limit the working power and produce irreversible surface damage in high-power rf components and rf sources.

Experimental work on high-gradient acceleration was a major part of early linear collider development; see, for instance, the work of Balakin *et al.* [7] and of Loew and Wang [8].

The work of Loew and Wang [8] considered that the rf breakdowns were directly linked to the peak electric field. They were studying the peak limit value of the electric field that generates breakdowns. Their work was carried out at different frequencies: S band, C band, and X band. They found that the maximum peak surface electric field achievable without rf breakdowns grows with the square root of the frequency. This analysis led to the idea that the maximum accelerating gradient, limited by breakdown, increases with the frequency. Later, other research carried out at CERN [9–11] in the frequency range from 21 to 39 GHz concluded that there is no increase in the maximum achievable gradient at higher frequencies. Both studies considered rf breakdown as a phenomenon generated when the peak electric field exceeds a certain threshold.

\*dalforno@slac.stanford.edu

Published by the American Physical Society under the terms of the Creative Commons Attribution 3.0 License. Further distribution of this work must maintain attribution to the author(s) and the published article's title, journal citation, and DOI.

Major studies to understand and mitigate the effects of rf breakdown were conducted during the development of the normal-conducting 11.424 GHz linear collider NLC/GLC [2,3,12], which has been replaced by the 12 GHz CERN-based linear collider CLIC [13]. Advances in understanding limitations on the accelerating gradient go beyond linear colliders. Accelerators are used in applications such as inverse Compton scattering gamma-ray sources [5], compact free-electron lasers (FELs) [14,15], and compact medical linacs for hadron therapy [16]. Modern high-gradient devices, such as photo-rf guns [17], fourth-harmonic linearizers for FELs [18], rf deflectors [19–21], and rf undulators [22,23], all use these technologies and methods, developed and sustained by studies of high-gradient accelerators.

During the NLC/GLC work, the statistical nature of rf breakdown became apparent [2,3,12,24]. For most accelerating structures exposed to the same rf power and pulse shape, the number of rf breakdowns per pulse is nearly steady or slowly decreasing over  $10^5$ – $10^7$  pulses. The breakdown probability became one of the main quantitative requirements characterizing high-gradient performance of linacs. For example, the CLIC linear collider requires the rf breakdown probability to be less than  $4 \times 10^{-7}$  per pulse per meter for a loaded accelerating gradient of 100 MV/m.

As technology progressed, sophisticated manufacturing and surface preparation techniques and systematic rf processing methods were developed [25–28]. As a result of this research and development, practical 11.4 GHz traveling-wave (TW) accelerating structures, which are CLIC prototypes, run at breakdown rates of about  $10^{-6}$  per pulse per meter at unloaded gradients up to 120 MV/m and  $\sim 200$  ns pulse length [29]. TW structures that include wakefield damping work at about 100 MV/m for similar breakdown rates [29,30]. Studies of new geometries and materials at 11.424 GHz show the potential to reach 150 MV/m accelerating gradients with similarly low breakdown rates [31].

Presently, X-band structures are the most studied in terms of rf breakdowns [24,32–35]. We know that breakdown statistics depend on pulsed surface heating [36] and a numerous list of other factors, such as the peak electric field, the peak magnetic field [37], and the peak Poynting vector [38]. In this paper, using all the knowledge and technologies developed in designing, fabricating, and testing for X-band structures, we want to explore the physics of rf breakdowns at subterahertz frequencies.

W-band metallic and dielectric structures were previously studied at SLAC by Whittum *et al.* [6,39–44]. Also, Hill *et al.* [45–48] tested both a single metallic W-band cavity and a dielectric linear accelerator excited with an electron beam. They studied the longitudinal and transverse wakefields in a 91 GHz dielectric-coated accelerating structure [49]. Henke and Bruns [50–53] and Chou and Kroll at SLAC designed a W-band muffin-tin planar

accelerator structure [54–56]. These studies highlight the difficulties of working at W-band frequencies. The challenge was to accurately manufacture and assemble the structure from its parts [57].

Another approach to reaching high accelerating gradients at higher frequencies involves dielectric wakefield accelerators. These schemes have been tested at SLAC FACET [58,59] and elsewhere [60–63]. At Argonne, beam-driven structures [64–67], both metallic and dielectric, were also tested. To our knowledge, in these experiments there were no systematic studies of the rf breakdown probability.

As a part of the high-gradient research at SLAC, we are studying rf breakdown physics in open metallic accelerating structures at 100 and 200 GHz frequencies. The results of the tests of the 100 GHz structures are presented in two papers [68,69]. Reference [68] reports the test results of 100 GHz copper and stainless steel accelerating structures. We found that the nondamage conditions in a 100 GHz copper traveling-wave accelerating structure is 0.3 GV/m, with a pulse length of 2.38 ns. As the studies progressed, we improved our diagnostic tools, by introducing the *arc-detector* diagnostic unique to our open metallic structures, used to measure the breakdown rate. The first results of the breakdown rate measurements are presented in Ref. [69]. Recent experiments carried out at Argonne [64] at 91 GHz used a similar open accelerating structure.

In this work, we used the techniques developed in our 100 GHz tests [68,69] to extend the studies of rf breakdowns to 200 GHz. In this paper, we present a quantitative measurement of rf breakdown rates and gradients in a 200 GHz copper and a copper-silver open traveling-wave accelerating structure. At the X band, it took thousands of hours of conditioning at repetition rates of 50 or 60 Hz to achieve the low breakdown rates required by linear colliders. Our FACET experiments are limited to a few shifts of several hours each, with repetition rate of up to 29 Hz; therefore, we could measure only statistically significant breakdown rates of about one breakdown per hundred pulses, which are much higher than the ones needed for FELs or colliders.

The 200 GHz accelerating structures were excited by an ultrarelativistic electron beam. The structures are constant impedance, open, consisting of two separate halves. To reduce field enhancement, all the cavity edges were rounded. With the open structure we were able to vary the gap between the two halves, changing the rf parameters. The FACET bunch charge was fixed during the experiment; therefore, we changed the gradient by varying the relative position of the beam with respect to the center of the structure. The two halves are insulated from each other and ground. They allow the realization of the arc detector, used to measure the field emission current and to reliably detect rf breakdowns. Details of the arc detector are described in the experimental chapter.

TABLE I. Symbols and abbreviations used in this papers.

$c$	Speed of light
$d$	Cell length period
$\Delta\phi$	Phase advance
$R$	Shunt impedance per unit length
$P_d$	Dissipated power in one cell
$U$	Stored energy in one cell
$P$	Power flow through the cavity cross section
$P_{\text{out}}$	Total power radiated from the two output horns
$\kappa_z$	Loss factor per unit length
$v_g$	Group velocity
$\tau_F$	Filling time
$\tau_D$	Decay time (of the rf power)
$\tau_T$	Equivalent pulse length with same peak pulsed heating
$\tau_W$	Equivalent pulse length with same pulse energy
$l_{\text{att}}$	Attenuation length
$V$	Integrated accelerating voltage
$E_{\text{acc}}$	Accelerating gradient
$E_{\text{max}}$	Peak electric field on surface
$H_{\text{max}}$	Peak magnetic field on surface
$Q_0$	Unloaded quality factor
$q$	Bunch charge
$\sigma_z$	rms bunch length
$L$	Length of the accelerating structure
$2a$	Gap size between the two halves
$e$	Electron charge
$\Delta x$	Horizontal beam displacement on the diagnostic screen
$\theta_x$	Horizontal kick angle
$V_x$	Deflecting voltage
$E$	Beam energy
$R_{12}$	Optics coefficient that converts a beam horizontal angle into a beam horizontal displacement
$\mu$	Magnetic permeability
$\sigma$	Electric conductivity
$k$	Thermal conductivity
$\rho$	Copper density
$c_e$	Specific heat

This paper is divided into three sections. In the first section, we show the geometry of the structure. In the second section, we present the rf and wakefield simulations, including the estimation of the pulsed surface heating. The third section reports experimental results and comparison with simulations.

All symbols used in this paper are presented in Table I.

## II. DESIGN AND GEOMETRY OF THE STRUCTURES

In our experiments we studied breakdowns in beam-driven 200 GHz copper and copper-silver accelerating structures. The copper-silver alloy contains 0.085% of silver. Since we do not have access to millimeter-wave rf sources, we designed wakefield-excited structures. The beam was generated by FACET [58], housed in the first 2 km of the SLAC linear accelerator [1]. During the experiments, the FACET beam energy was 20.35 GeV.

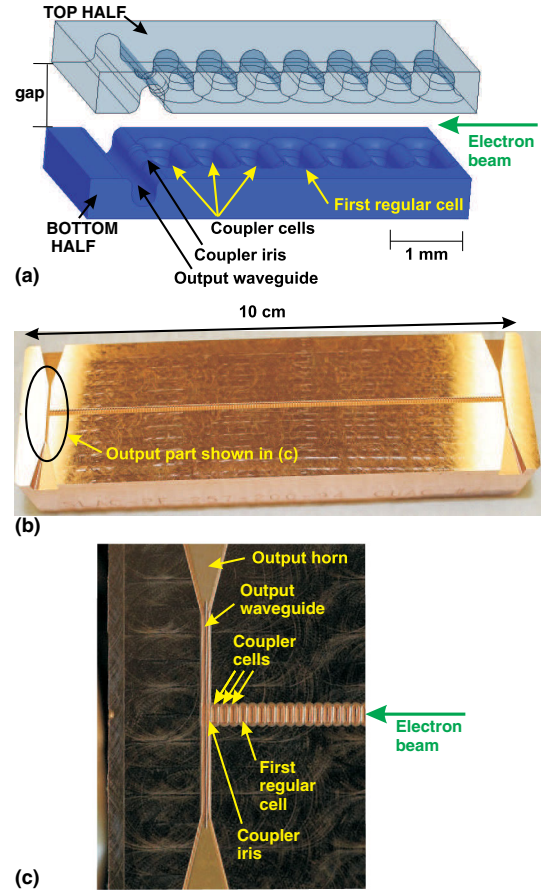


FIG. 1. Solid model of the output section of the 200 GHz traveling-wave accelerating structure (a), picture of one-half of the Cu-Ag structure (b), and picture of the output section of the structure (c).

In the experiment with the copper structure, the bunch charge was 3.2 nC, the bunch length  $\sigma_z$  was 50  $\mu\text{m}$ , and the repetition rate varied from 1 to 15 Hz. In the experiment involving the copper-silver structure, the bunch charge was 1.6 nC, the bunch length  $\sigma_z$  was 25  $\mu\text{m}$ , and the repetition rate was 29 Hz.

In the design and realization of the 200 GHz structure, we benefit from the experience achieved for the 100 GHz ones. We designed the accelerating structures to be open type, composed of two separate movable metal halves. The horizontal position, the vertical position, and the gap are remotely controlled by three movers. The cavities and couplers are milled into the flat side of metal blocks. When the two halves are placed together, they form a single accelerating structure. The regular cell has been designed to have  $5\pi/6$  phase advance when the gap is set to 0.3 mm. The choice of the phase advance comes from our experience with manufacturing the 100 GHz accelerating structures. We kept the iris thickness similar in both cases, and we increased the beam synchronous frequency by increasing the phase advance with a manufacturable cell period  $d$ . The gap  $2a = 0.3$  mm was chosen to accommodate the

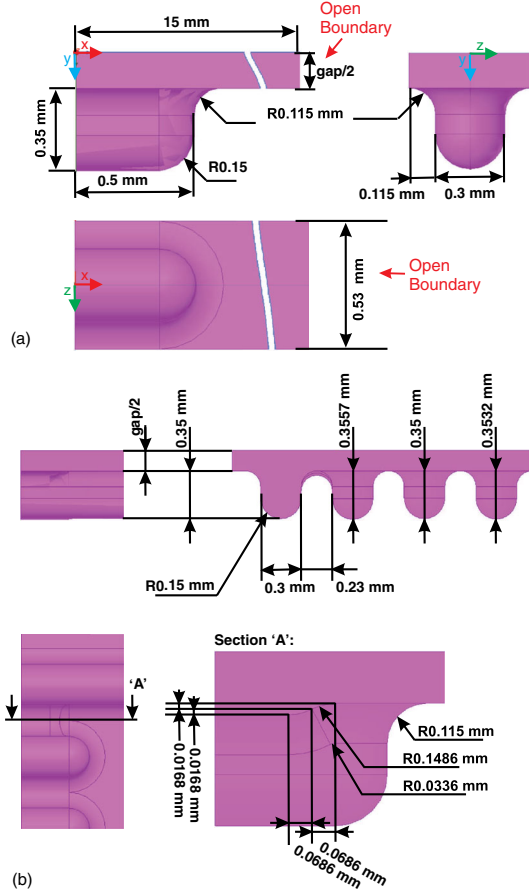


FIG. 2. Geometry of one-quarter of the vacuum part of the regular cell (a) and of the rf power coupler of the structure (b).

practical transverse bunch size in our 100 GHz experiments.

All the edges have been rounded to minimize the peak fields. The rf parameters of the structure can be changed by varying the gap. Both input and output couplers are symmetric dual feed, radiating energy out through antenna horns towards pyrodetectors. The whole structure is 10 cm long, with an active length of the accelerating cavities of 8.85 cm. There are 161 regular cavities and two couplers with three matching cells each.

Figure 1(a) shows the solid model of the output section of the 200 GHz traveling-wave accelerating structure, Fig. 1(b) shows a picture of one-half of the copper-silver structure, and Fig. 1(c) shows a picture of the output section of the structure. When the gap is closed the structure has no beam pipe, the two blocks are in contact with each other, and there is no opening for the beam to travel. The geometry of the vacuum part of the regular cell is shown in Fig. 2(a), while the coupler is in Fig. 2(b).

### III. RF SIMULATIONS

In our experiments, the electromagnetic fields in the structure are excited by the FACET ultrarelativistic electron

beam. To characterize the beam-structure interaction, we used the rf simulation code Ansys HFSS [70] to calculate the rf parameters, accelerating gradients, and peak fields. Those quantities were calculated by simulating one period of the regular cell. The calculation method is described in Ref. [68]. The following relations are used to obtain the rf quantities that characterize the structure.

The shunt impedance per unit length is

$$R = \frac{V^2}{P_d d}. \quad (1)$$

The loss factor (per unit length) including the group-velocity-related compression factor [71–73] is

$$\kappa_z = \frac{V^2}{4U} \frac{1}{d} \frac{1}{1 - v_g/c}. \quad (2)$$

The group velocity is

$$v_g = P/(U/d). \quad (3)$$

The decay time (of the rf power) is

$$\tau_D = \frac{Q_0}{\omega_0} \left(1 - \frac{v_g}{c}\right). \quad (4)$$

The attenuation length is

$$l_{att} = \frac{P}{P_d} d \left(1 - \frac{v_g}{c}\right) = v_g \tau_D. \quad (5)$$

The filling time is

$$\tau_F = \frac{L}{v_g} \left(1 - \frac{v_g}{c}\right). \quad (6)$$

After calculating the above rf parameters, the following expressions are the quantities induced by the beam, for a given mode.

The induced accelerating gradient is

$$E_{acc} = 2\kappa_z q \exp\left(-\frac{\omega_0^2 \sigma_z^2}{2c^2}\right). \quad (7)$$

The induced power flow is

$$P = \kappa_z q^2 v_g \frac{1}{1 - v_g/c} \exp\left(-\frac{\omega_0^2 \sigma_z^2}{c^2}\right). \quad (8)$$

The pulse energy is

$$W = \int_0^{\tau_F} P \exp\left(-\frac{t}{\tau_D}\right) dt = P \tau_D \left[1 - \exp\left(-\frac{\tau_F}{\tau_D}\right)\right]. \quad (9)$$

The rf parameters of the fundamental accelerating mode are listed in Table II. The quality factor  $Q_0$  was calculated

TABLE II. rf parameters of the regular cell of the 200 GHz structure, for the fundamental mode, excited by a 1 nC bunch with  $\sigma_z$  of 50  $\mu\text{m}$ .

Gap [mm]	$f$ [GHz]	$\Delta\phi$ [deg]	$Q_0$	$R$ [ $M\Omega/\text{m}$ ]	$\kappa_z$ [MV/(nC m)]	$v_g/c$ [%]	$l_{\text{att}}$ [mm]	$P$ [MW]	$E_{\text{acc}}$ [GV/m]	$E_{\text{max}}$ [GV/m]	$H_{\text{max}}$ [MA/m]
0.3	237.9	151	1521	305	74.1	1.88	5.63	0.40	0.144	0.40	0.77
0.5	223.9	143	1566	195	46.5	8.54	26.1	1.23	0.090	0.31	0.63
0.7	215.4	137	1642	126	30.7	17.7	52.9	1.88	0.060	0.26	0.53
0.9	209.2	133	1742	84.7	21.3	26.9	78.2	2.25	0.042	0.22	0.46
1.1	204.3	130	1861	59.1	15.4	35.4	99.3	2.41	0.030	0.20	0.40
1.3	200.4	128	1995	42.8	11.5	42.7	116.3	2.47	0.023	0.18	0.36
1.5	197.0	125	2142	31.9	8.86	49.1	129.7	2.46	0.017	0.16	0.32

by using the copper resistivity and by assuming it to be the same as for the copper-silver. From our X-band experiments, the copper-silver structure has practically the same  $Q_0$  as the copper one.

### A. Coupler matching

Practically, the rf coupler can be designed to be matched only for a specific gap size. We choose to match the coupler at a 0.3 mm gap size and find afterwards the reflectivity for other gap values. The matching procedure is described in Refs. [74,75]. In this exercise, we varied the gap from 0.2 to 1.5 mm. Figure 3 shows the reflection and power transmission of the coupler for different gap sizes.

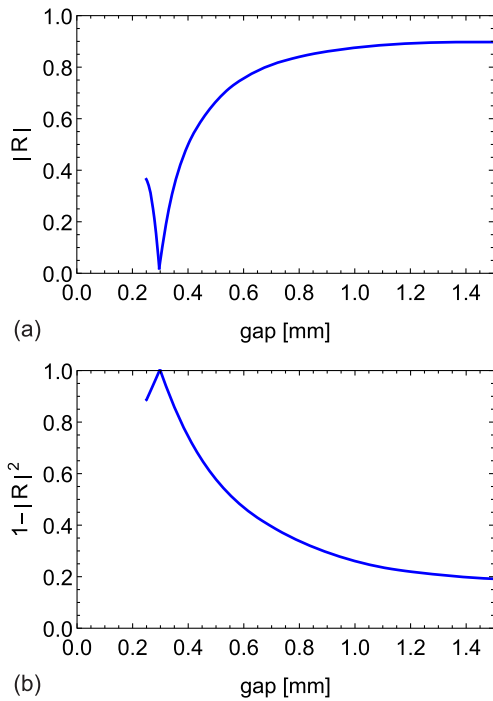


FIG. 3. Coupler reflection (a) and power transmission (b) as a function of the gap aperture, calculated with the coupler matched at the 0.3 mm gap.

### B. Radiated power through the output waveguide

With a gap size of 0.3 mm, all the rf power is coupled to the output waveguide. For the other gaps, the power of the fundamental mode radiated from the waveguides is calculated by taking into account the reflection in the following way:  $P_{\text{out}} = P(1 - |R|^2)$ , where the reflection of the other upstream coupler is ignored. The rf power pulses generated by the 3.2 nC bunch, with  $\sigma_z = 50 \mu\text{m}$ , are depicted in

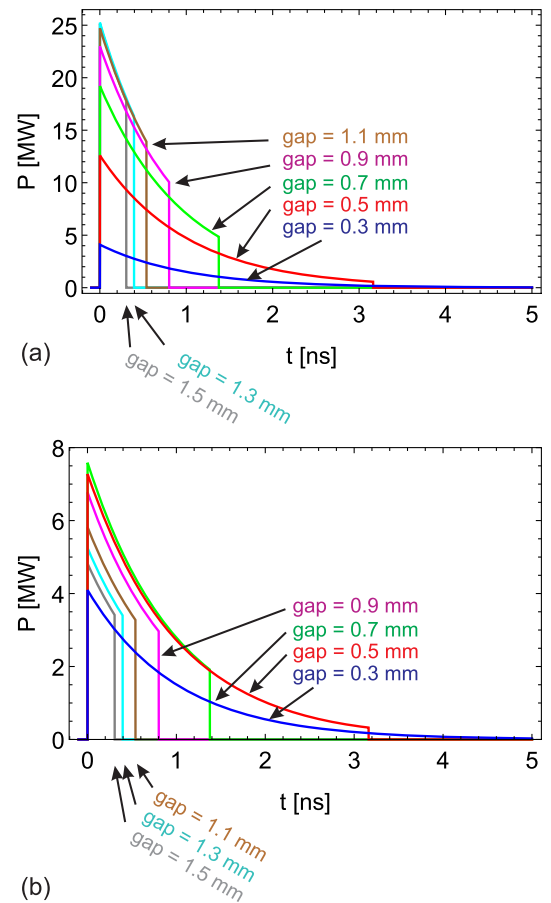


FIG. 4. Output rf power signals generated by a 3.2 nC bunch of 50  $\mu\text{m}$ , without coupler reflections (a) and taking into account the coupler reflection (b). The pulse rf durations depends on the group velocity, structure length, and attenuation.

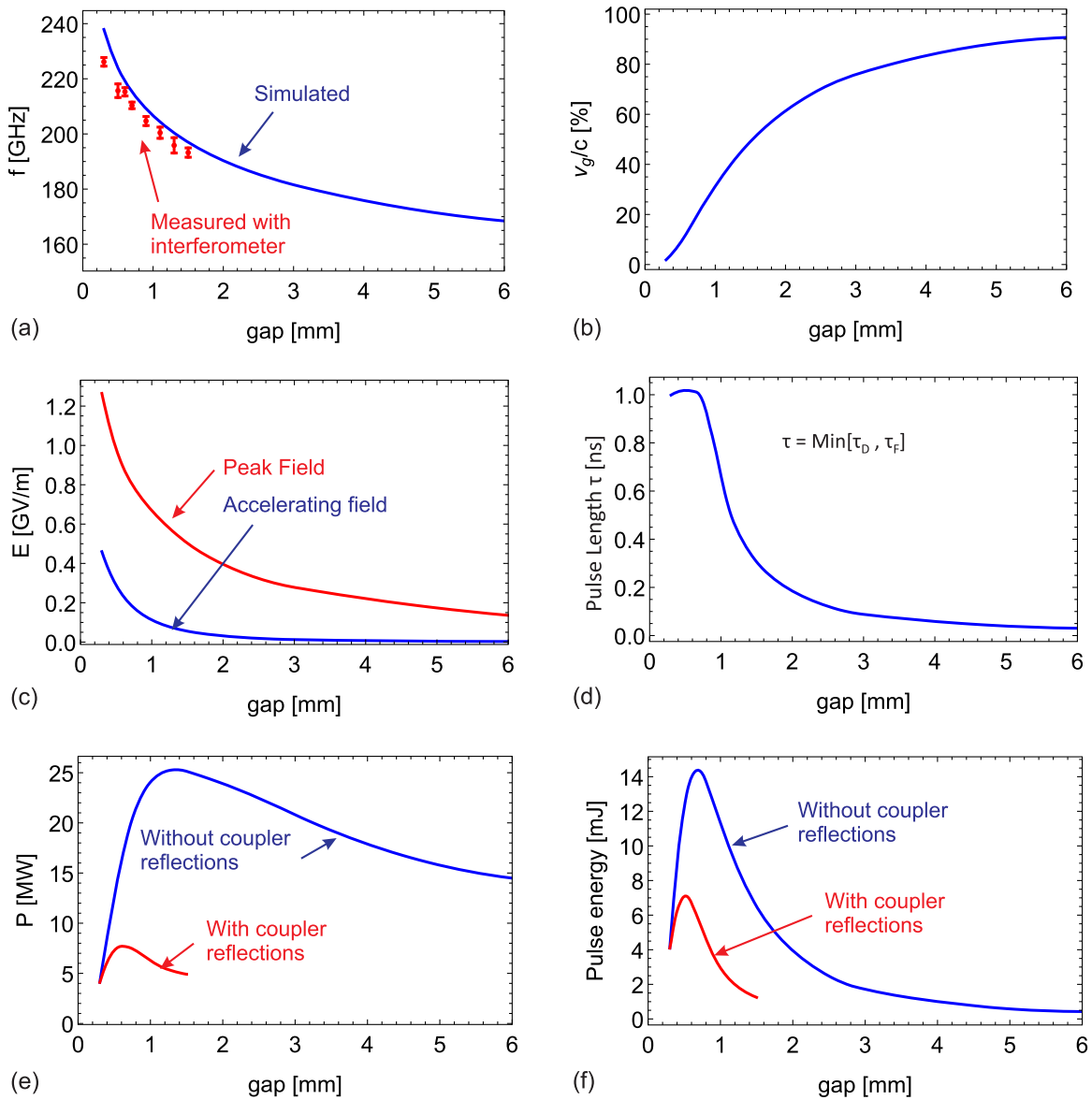


FIG. 5. Plot of the synchronous frequency (a), group velocity (b), accelerating and peak electric field of the fundamental mode (without considering the coupler reflections) (c), pulse length (d), peak power traveling along the cells and power exiting from the waveguides considering the coupler reflection (e), and pulse energy with and without considering the coupler reflection (f). The electron beam is in the central axis; by opening the gap, the field is reduced because the interaction decays. The bunch charge is 3.2 nC, and  $\sigma_z = 50 \mu\text{m}$ .

Fig. 4, without the coupler reflection (a) and with the coupler reflection (b). The rf output power per each horn is  $P_{\text{out}}/2$ , due to the symmetric dual feed coupler type.

### C. rf parameters

In the following, we present a series of plots that describe the results of the rf simulations for the 200 GHz copper traveling-wave accelerating structure. The plot of the frequency, group velocity, electric field (accelerating and peak on surface), pulse length [as the minimum between the decay time ( $\tau_D$ ) and the filling time ( $\tau_F$ )],

power, and pulse energy of the fundamental mode are in Fig. 5, with 3.2 nC of bunch charge and  $\sigma_z = 50 \mu\text{m}$  as a function of the gap size (assuming the beam in the central axis).

### D. Pulsed surface heating

Cyclic thermal stresses produced by rf pulsed heating were identified as a limiting factor for linear accelerators at extremely high frequencies [76–78]. Pulsed surface heating limited the performance of accelerator couplers at X-band linear accelerators considered for the NLC [2,3,12,24].

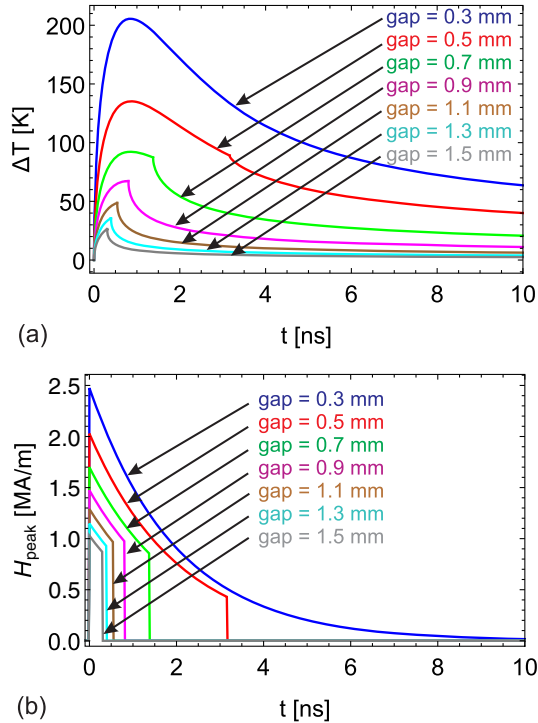


FIG. 6. Temperature variation in a cell, generated by a 3.2 nC bunch of  $50 \mu\text{m}$ , without taking into account the coupler reflections (a) and surface peak magnetic field as a function of the time (b).

Recent studies of breakdown rates in high-gradient linear accelerators showed a direct correlation between these rates and pulsed heating [79].

The correlation of peak pulsed surface heating with rf breakdowns motivated us to evaluate the pulsed surface heating in the beam-excited 200 GHz accelerating structures. We analyzed the pulsed heating in a regular cell located near the output coupler by using the following assumptions. We consider fields of only the fundamental mode, without taking into account coupler reflections; therefore, we did not consider the increase of pulsed heating due to standing waves caused by coupler reflections. We assumed that there was no increase of conductivity due to surface roughness and that the metal physical properties did not change during the rf pulse. In the calculations of pulsed heating for copper-silver, we used the properties of copper, since a small percentage of silver in the copper does not significantly change the material properties.

The time-dependent pulsed surface heating is calculated by using [36,78]

$$\Delta T(t) = \frac{1}{2} \sqrt{\frac{f\mu}{k\sigma\rho c_e}} \int_0^t \frac{H(t')^2}{\sqrt{t-t'}} dt', \quad (10)$$

where  $H(t)$  is the time-dependent peak surface magnetic field,  $f$  is the working frequency,  $\mu$  is the magnetic permeability of copper,  $\sigma$  is the electric conductivity of

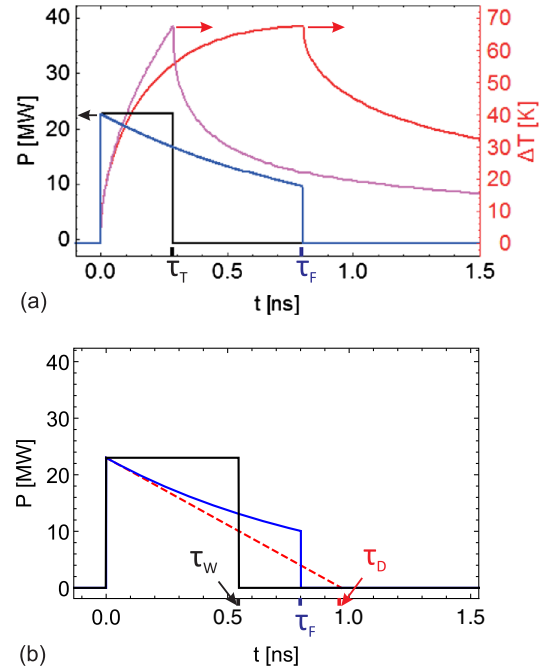


FIG. 7. Derivation of equivalent pulse lengths for gap = 0.9 mm, a field generated by a 3.2 nC bunch of  $50 \mu\text{m}$  (without taking into account the coupler reflections). (a) The blue plot is the power pulse generated by the electron beam in the regular cell of the structure. The corresponding pulsed surface heating is the magenta plot, that reaches 67 K of peak pulsed heating. The black pulse is the equivalent square pulse “in temperature,” with pulse length  $\tau_T$ , which produces the same peak pulsed heating as the beam-generated rf pulse. Note that  $\tau_T$  is calculated under the constraint that the blue and black rf pulses have the same max power (at  $t = 0$ ). The red plot is the pulsed heating generated by the square pulse. (b) The blue plot is the power pulse generated by the electron beam in the regular cell of the structure. The black pulse is the equivalent square pulse “in energy,” with pulse length  $\tau_W$ , which has the same pulse energy and same max power (at  $t = 0$ ) as the blue. The red plot is used to illustrate the power decay time  $\tau_D$ : it is the ordinate intercept of a line tangent at  $t = 0$  to the beam-excited power.

copper,  $k$  is the thermal conductivity of copper,  $\rho$  is the copper density, and  $c_e$  is the specific heat of copper. For a square rf pulse, with amplitude  $H(t) = H_{\text{max}}$  and pulse length  $\tau$ , the peak pulsed heating is given by

$$\Delta T = \sqrt{\frac{f\mu}{k\sigma\rho c_e}} |H_{\text{max}}|^2 \sqrt{\tau}. \quad (11)$$

In our experiment, the pulse of the fundamental mode near the output coupler decays exponentially and is truncated by the filling time  $\tau_F$  (see Fig. 4). Thus, the behavior of  $H(t)$  can be modeled as

$$H(t) = \begin{cases} 0 & t < 0, \\ H_{\text{max}} e^{-t/(2\tau_D)} & 0 < t < \tau_F, \\ 0 & t > \tau_F, \end{cases} \quad (12)$$

TABLE III. Pulsed heating and equivalent pulse lengths for the Cu experiment, with 3.2 nC of bunch charge and  $\sigma_z = 50 \mu\text{m}$ , and for the CuAg experiment, with 1.6 nC of bunch charge and  $\sigma_z = 25 \mu\text{m}$ .

Gap [mm]	$f$ [GHz]	$E_{\text{acc}}$ [GV/m]		$E_{\text{max}}$ [GV/m]		$H_{\text{max}}$ [MA/m]		Peak pulsed heating [K]					
		Cu	CuAg	Cu	CuAg	Cu	CuAg	Cu	CuAg	$\tau_D$ [ns]	$\tau_F$ [ns]	$\tau_T$ [ns]	$\tau_W$ [ns]
0.3	237.9	0.46	0.241	1.26	0.65	2.47	1.28	205.47	55.09	1	15.4	0.3	1
0.5	223.9	0.289	0.151	0.98	0.51	2.03	1.05	135.18	35.96	1	3.16	0.3	0.97
0.7	215.4	0.192	0.1	0.82	0.42	1.7	0.87	92.2	24.41	1	1.38	0.29	0.75
0.9	209.2	0.133	0.069	0.71	0.37	1.47	0.76	67.3	17.76	0.97	0.8	0.28	0.55
1.1	204.3	0.096	0.05	0.63	0.32	1.29	0.66	48.65	12.81	0.94	0.54	0.26	0.41
1.3	200.4	0.072	0.037	0.56	0.29	1.15	0.59	35.61	9.36	0.91	0.4	0.23	0.32
1.5	197.0	0.056	0.029	0.5	0.26	1.03	0.53	26.35	6.91	0.88	0.31	0.19	0.26

which can be integrated analytically. The calculations of the peak pulsed surface heating in the cell, generated by a 3.2 nC bunch with  $\sigma_z = 50 \mu\text{m}$ , are shown in Fig. 6(a), for different gaps. Figure 6(b) shows the surface peak magnetic field as a function of the time, for the pulse shapes shown in Fig. 4(a).

### E. rf pulse length

In X-band structures, there is a strong dependence of the breakdown rate on pulse length [24,32]. In beam-excited structures, the pulse is decaying. Therefore, it is hard to compare the results with previous data obtained with

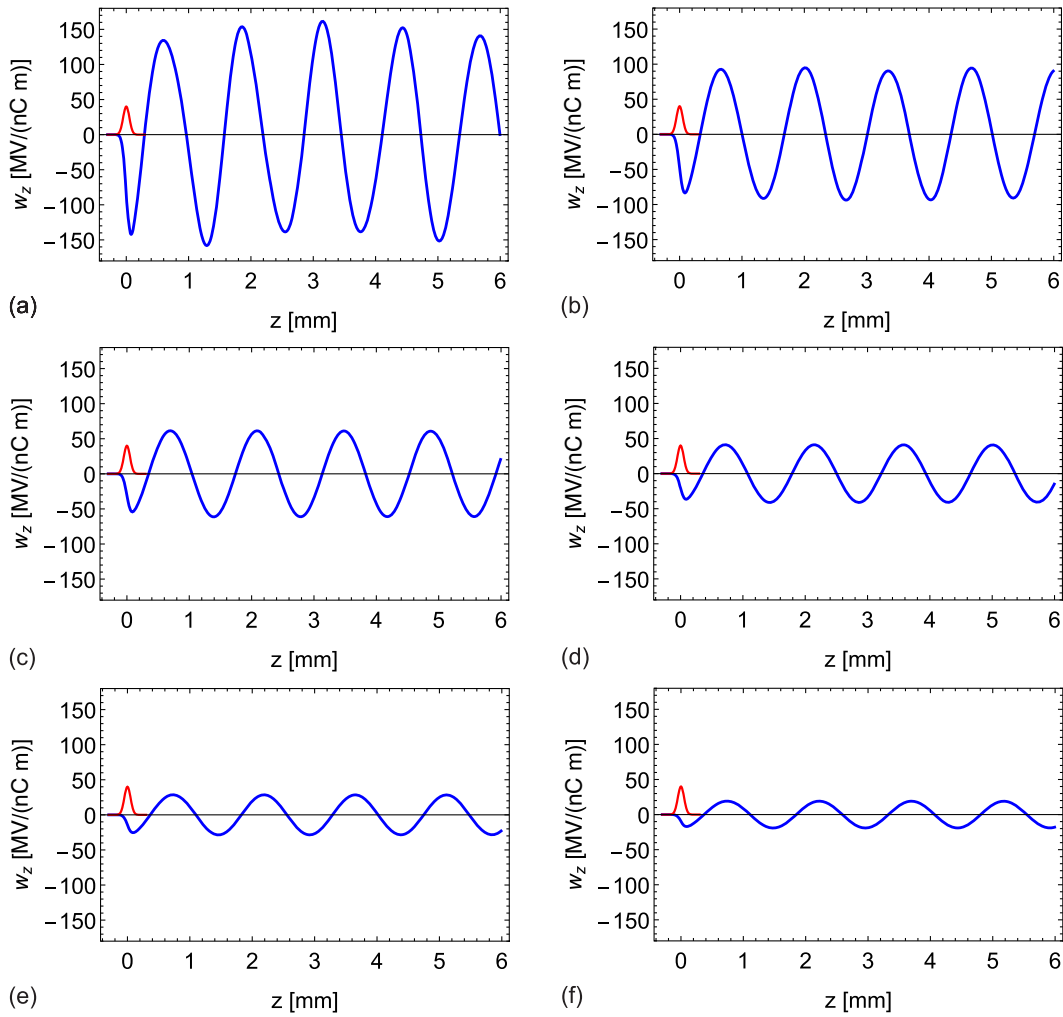


FIG. 8. Longitudinal decelerating wakefield (blue curve), electron bunch shape (red curve), of the 235 GHz structure, for 0.3 mm gap (a), for 0.5 mm gap (b), for 0.7 mm gap (c), for 0.9 mm gap (d), for 1.1 mm gap (e), and for 1.3 mm gap (f), calculated using the HFSS+Mathematica method [68].

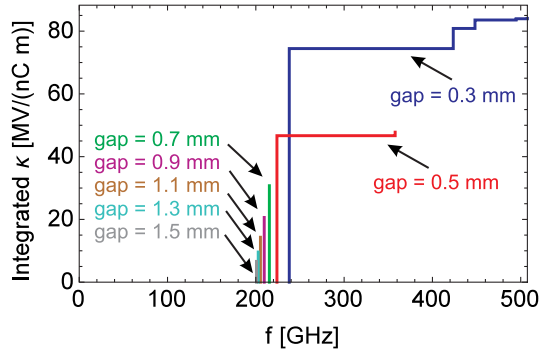


FIG. 9. Integrated loss factors for the TW structure, with  $\sigma_z = 50 \mu\text{m}$ , for all the analyzed gaps, with the electron beam on axis.

structures excited by rf sources, such as klystrons. In order to compare our results with results of structures excited by rf sources, we introduced two quantities related to pulse length. We defined  $\tau_T$  as the equivalent pulse length which procures the same surface heating as a rectangular one and  $\tau_W$  as the equivalent pulse length with the same pulse energy.

The equivalent pulse length with the same peak pulsed surface heating ( $\tau_T$ ) is calculated as the pulse length of a square pulse that gives the same peak pulsed heating as calculated with the beam-excited pulse, with the constraint that the peak power is the same.

The equivalent pulse length with the same pulse energy ( $\tau_W$ ) is calculated as the pulse length of a square pulse that

has the same energy of the beam-excited pulse, with the constraint that the peak power is the same.

The four pulse lengths ( $\tau_D$ ,  $\tau_F$ ,  $\tau_T$ ,  $\tau_W$ ) are shown in Fig. 7, for gap = 0.9 mm, generated by a 3.2 nC bunch of  $50 \mu\text{m}$  (without taking into account the coupler reflections).

We show in Table III the pulsed surface heating and equivalent pulse lengths for the Cu experiment, with 3.2 nC of bunch charge and  $\sigma_z = 50 \mu\text{m}$ , and for the CuAg experiment, with 1.6 nC of bunch charge and  $\sigma_z = 25 \mu\text{m}$ .

## F. Long-range wakefields

We calculated the long-range wakefields and the accelerating gradients induced by the electron bunch at different gap sizes. We used the HFSS+*Mathematica* method explained in Ref. [68]. The results are shown in Fig. 8.

The integrated loss factor is shown in Fig. 9, for different gaps, considering  $\sigma_z = 50 \mu\text{m}$ .

## G. Short-range wakefields

We performed the short-range wakefield simulations, and we measured the deflecting voltage by observing the displacement of the electron beam on a diagnostic screen. This allowed us to confirm the simulated gradients. When the electron beam trajectory moves horizontally off axis, it excites deflecting fields; however, when the beam trajectory moves far beyond the corrugations, the deflection disappears. We simulated wakefields excited by a

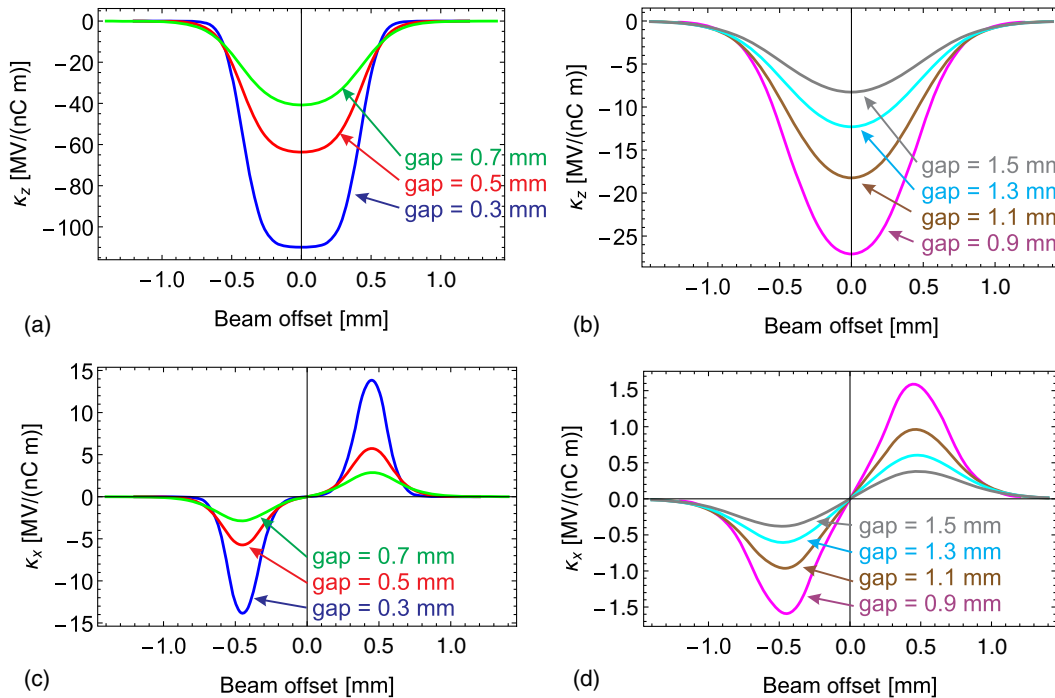


FIG. 10. Loss factor (a),(b) and kick factor (c),(d) as a function of the horizontal beam-structure displacement, for different gaps. The fields are generated by a  $\sigma_z = 50 \mu\text{m}$  bunch in a 10 cm long structure.

Gaussian bunch with  $\sigma_z = 50 \mu\text{m}$  (used in the copper structure) by using CST Particle Studio [80]. The loss factor and the kick factor in the 235 GHz structure are shown in Fig. 10.

These results are in good agreement with the wakefield calculations made with GdfidL [81] and the NOVO code, developed by Novokhatski [82–85].

#### IV. EXPERIMENTAL SETUP AND RESULTS

In this section, we show the experimental results for the two accelerating structures. The FACET electron beam had an energy of 20.35 GeV. We had three shifts. In the first two (April 25–27, 2015) we used the copper structure, the bunch charge was 3.2 nC,  $\sigma_z = 50 \mu\text{m}$ , and the repetition rate varied from 1 to 15 Hz. The third shift (May 15, 2015) involved the copper-silver structure, the bunch charge was 1.6 nC,  $\sigma_z = 25 \mu\text{m}$ , and the repetition rate was 29 Hz.

##### A. Installation of the accelerating structures

The structures, and the remote controlled stages used to align the structures to the beam, were housed in a vacuum chamber in the FACET experimental area, shown in Fig. 11. A camera located after the vertically bending magnet records the screen image of the bunch at each pulse. The vertical screen coordinate corresponds to the beam energy. The beam optics between the test structure and the camera converts the horizontal kick angle  $\theta_x$ , generated by the structure, to a horizontal beam displacement  $\Delta x$ , given by

$$\Delta x = R_{12} \cdot \theta_x = R_{12} \cdot \frac{eV_x}{E},$$

where  $R_{12}$  ( $=14 \text{ m}$ ) is the optics coefficient that converts a beam horizontal angle into a beam horizontal displacement, given by the deflecting voltage  $V_x$  and the beam energy  $E$ . By measuring  $\Delta x$  on the diagnostic screen, the deflecting voltage is determined. In this measurement, we assume that the 20 GeV beam does not receive an offset shift at the end of the structure. It receives only a change in the angle trajectory.

In the installation process, we assembled the two halves of the accelerating structure on remotely controlled motorized stages. Motorized stages are used to shift the structure horizontally or vertically with respect to the electron beam. There was also a motor to adjust the gap between the two halves of the structure, shown in Fig. 12(b). The structure was aligned to the beam trajectory by backreflecting a reference laser, aligned to the beam trajectory, off of a

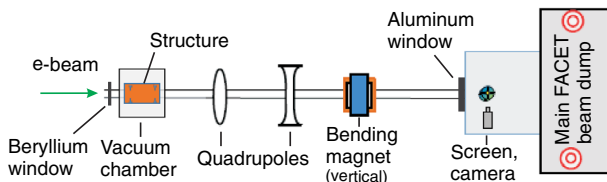


FIG. 11. Schematic of the experimental FACET section.

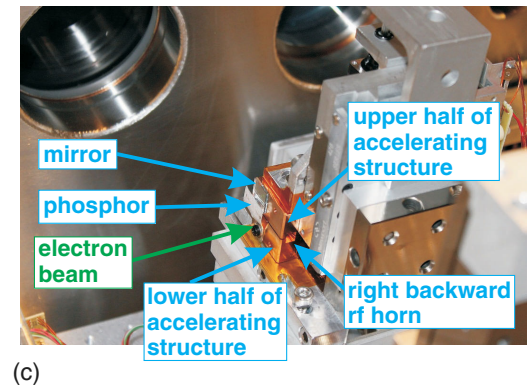
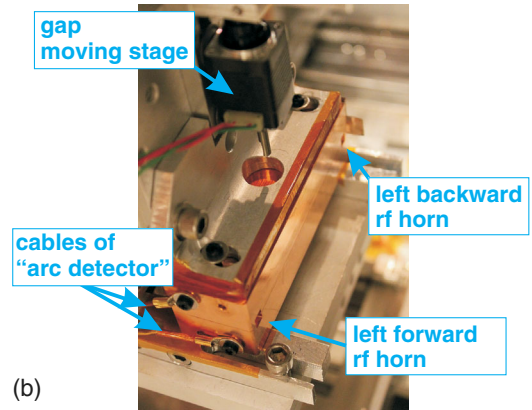
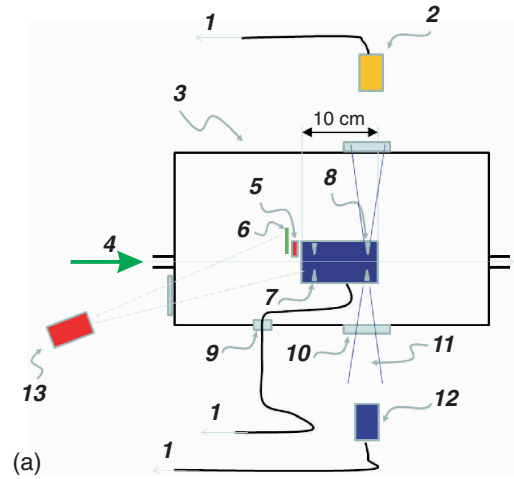


FIG. 12. Schematic of the experimental setup (a): signal to scope (1), interferometer (2), vacuum chamber (3), electron beam (4), laser alignment mirror (5), phosphor screen (6), right reflected rf horn (7), left forward rf horn (8), vacuum feedthrough (9), rf window (10), output rf beam (11), pyrodetector (12), and video camera for beam-structure alignment and rf breakdown diagnostic (13). The accelerating structure was assembled on remotely controlled motorized stages, with the arc-detector cables connected (b). The accelerating structure was installed in the vacuum chamber (c).

mirror attached to the structure [see Fig. 12(c)]. This alignment allows the electron beam to pass cleanly through the gap between the top and bottom halves of the structure. A phosphor screen is attached to detect the position

of the electron beam. The two forward output horns radiate the rf power. One output goes to the pyrodetectors and the other to the interferometer [see Fig. 12(a)].

For each experiment we recorded the pyrodetector voltage, which is proportional to the pulse energy emitted from the output waveguide horn.

In our 100 GHz experiments, we invented a new diagnostic tool able to reliably detect breakdowns [68]. Since breakdowns generate electron and ion currents, we built an arc detector unique to open structures. The two metal halves that compose the structure were electrically insulated from the ground and each other using a plastic film. We measured the field emission current and the breakdown current by measuring the voltage induced in the two separate metal blocks. This was achieved by connecting the two metal halves to an oscilloscope. A signature of a rf breakdown is a spike in the current monitor signal. We can clearly see voltage spikes of both polarities correlated with the transverse position of the electron beam inside the cavity and the magnitude of the pyrodetector signal. We assumed that these voltage spikes are due to currents generated by rf breakdowns.

The raw signal generated by the pyrodetectors and by the arc detector are processed by a boxcar integrator. A boxcar integrator (other names are gated integrator and boxcar averager) integrates the signal input voltage after a defined waiting time (trigger delay) over a specified period of time (gate width).

We show typical current monitor and pyrodetector signals, recorded with an oscilloscope, before the boxcar processing, in Fig. 13. There are three cases: no breakdowns (a), a breakdown that generated a positive signal (b), and a breakdown that generated a negative signal (c).

## B. Common experimental procedure

In this subsection, we describe the three common operations carried out during each experiment: operations before a beam, operation with a beam, and inspections after a beam exposure.

The common operations before beam are (i) machining: the structures were manufactured by the company EDM Department Inc. [86]; (ii) cleaning: the structures are cleaned according to SLAC procedure developed for the high-gradient X-band program; (iii) installation: the structure is installed on motorized stages that control the horizontal position, vertical position, and the gap. The assembly is then installed in the experimental vacuum chamber. A mirror is glued to the structure for laser alignment, and a phosphor screen is bolted to the edge of the structure to image the electron beam. The antenna horns of the structure are directed towards pyrodetectors that sense the pulse energy and towards an interferometer that measures the frequency spectrum of the emitted radiation. (iv) Alignment with the laser: a laser beam is aligned to the trajectory of the FACET electron beam from the previous run. We moved the structure

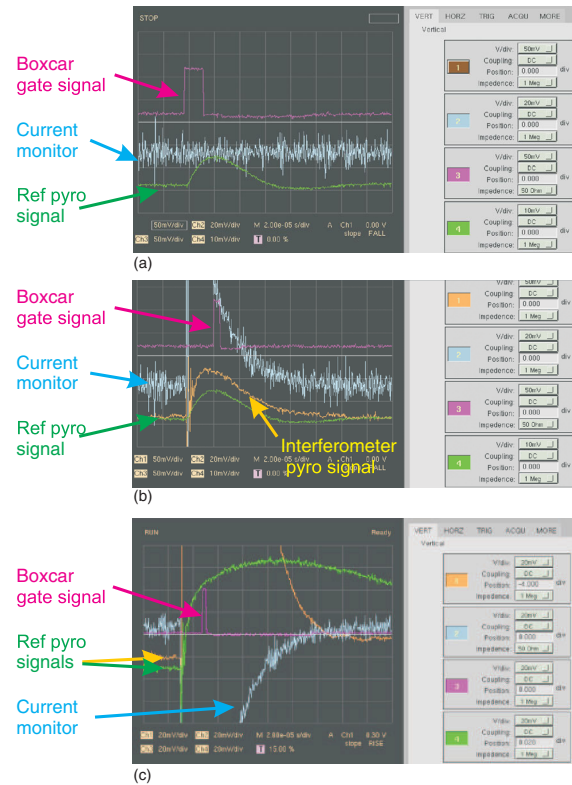


FIG. 13. Oscilloscope signals with no breakdowns (a), a breakdown that generated a positive signal (b), and a breakdown that generated a negative signal (c).

until the laser beam hit the mirror and then started the alignment procedure by tilting the structure with pitch screws. The structure is considered aligned when the reflected laser beam travels back along the same trajectory as the forward laser beam. (v) Pumping: the vacuum chamber is closed to establish a vacuum.

Operations with the electron beam are the following. (i) Detect the beam on the phosphor screen: if the electron beam hits the copper structure, it will cause damages to the delicate part of the corrugations. Therefore, as a first step, we must steer the beam onto the phosphor screen, which is installed far from the corrugations. (ii) Finding the vertical center of the structure: when the gap is set, we determine the vertical position of the structure that centers the beam vertically centered. This is done by setting the electron beam at an approximate vertical center (horizontally, it is far from the corrugations). The structure is slowly moved up (and down), till the beam slightly touches the copper, generating a radiation shower, detected by the accelerator control system. The vertical center is calculated taking the average between these upper and lower limits. (iii) Horizontal scan: once we determined the vertical center, the structure is moved horizontally, allowing the beam to interact with the corrugations, generating electromagnetic fields. During each scan, we observed the magnitude of the energy pulses produced by the structure with pyrodetectors. Breakdowns are detected

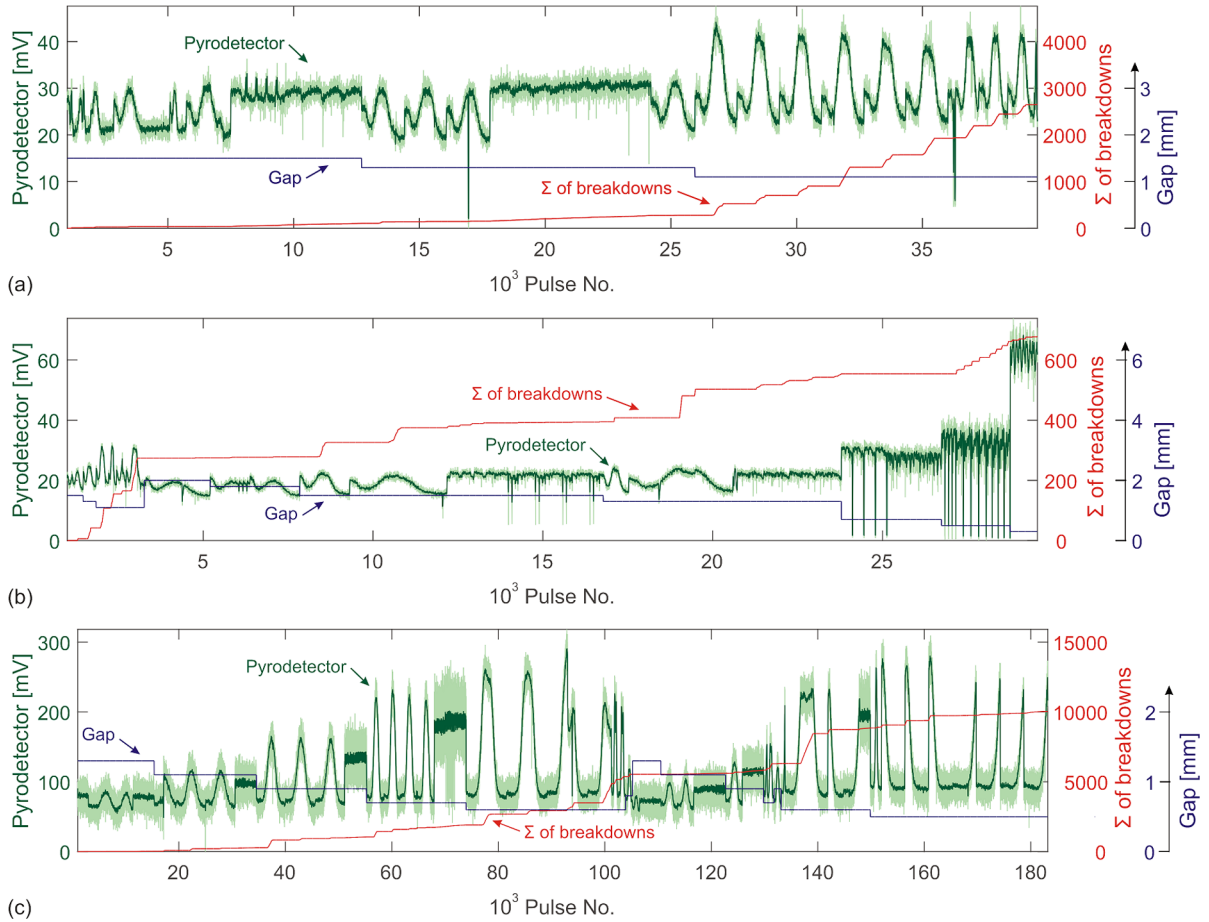


FIG. 14. Timeline of the experiments with the 200 GHz traveling-wave accelerating structures, copper structure with 3.2 nC of bunch charge and  $\sigma_z = 50 \mu\text{m}$  (a),(b) and copper-silver structure with 1.6 nC of bunch charge and  $\sigma_z = 25 \mu\text{m}$  (c). The green plot is the reference pyrodetector signal, the blue is the gap, and the red is the integrated number of breakdowns, recorded with the arc detector. Bell-shaped curves of the pyrodetector signal are generated during the scans of the beam over the cavities, and flat parts are the time intervals when we performed frequency measurements and collection of breakdowns.

using the arc-detector setup, as the gradient is varied. (iv) The scan procedure is then repeated with different gaps. (v) Constant gradient breakdown rate measurement: the beam is placed in the central axis. Breakdowns are counted using the arc detector, while the frequency is measured with the interferometer.

The after-beam operations are (i) the structure is removed and brought to the laboratory for inspection, and (ii) the structure is inspected with SEM, looking for signs of damage due to rf breakdowns. The position of each damage is then noted.

### C. Timeline of the experiments

In this section, we report the complete timeline of the experiments with the 200 GHz traveling-wave accelerating structures. Here we followed the format established for X-band rf breakdown experiments. We show the full history of the exposure of the structure to rf fields and the corresponding behavior of the accumulated rf breakdowns. Figures 14(a) and 14(b) show the data for the copper

structure with 3.2 nC of bunch charge and  $\sigma_z = 50 \mu\text{m}$  and Fig. 14(c) the data for the copper-silver structure with 1.6 nC of bunch charge and  $\sigma_z = 25 \mu\text{m}$ . We note that the largest number of pulses in the copper-silver structure is due to the higher repetition rate.

### D. Experimental results with the 235 GHz traveling-wave copper structure

In the experiments involving the copper structure (April 25–27, 2015), the bunch charge was 3.2 nC,  $\sigma_z = 50 \mu\text{m}$ , and the repetition rate varied from 1 to 15 Hz. We performed several horizontal scans, frequency measurements with interferometers, and breakdown rate statistics. The gap varied from 1.5 to 0.3 mm.

#### 1. Measurement of pulse energy with pyrodetector

At first, as the structure is moved along the horizontal direction, the beam crosses the structure where the corrugations are not present. By further moving the structure along the horizontal direction, the corrugations intercept

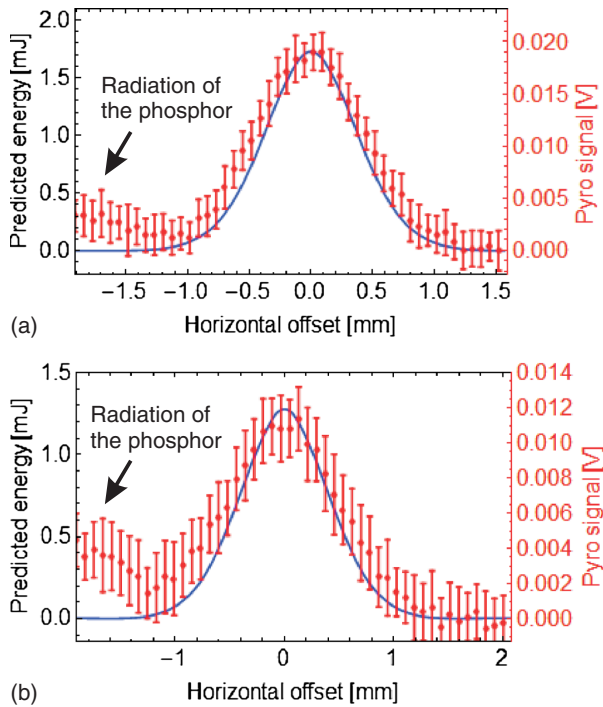


FIG. 15. Predicted (blue curve) and measured with the interferometer pyrodetector (red) pulse energy in a function of the horizontal position of a 3.2 nC electron beam, for the copper structure with gap = 1.3 mm (a) and gap = 1.5 mm (b).

the field of the electron beam, generating a power flux and an accelerating gradient. The maximum gradient occurred when the beam is on the structure axis. When the beam is moved further from the corrugations, the gradient decreases. The pulse energy of the output signal was measured with a pyrodetector. Two pulse energy measurements are shown in Fig. 15 (gap = 1.3 mm and gap = 1.5 mm) and compared with predicted values. The comparison between predicted and measured pulse energy as a function of the beam position is qualitative.

The interaction of the electron bunch with objects in our beam line generates wakefields in addition to the wakefields generated in our accelerating cavities. The bunch enters the chamber through a vacuum window, made of 50  $\mu\text{m}$ -thick beryllium foil, then passes through the input beam pipe, entering in the experimental chamber. The bunch then passes through the input and output face of our accelerating structure, which includes the phosphor screen, and exits the chamber, going through the beam pipe until finally exiting through a vacuum-to-air aluminum window (see Figs. 11 and 12). The electron bunch, passing through the beryllium and aluminum windows and through the phosphor screen, generates the so-called transition radiation. On other interfaces, it generates the diffraction radiation. This radiation can be picked up by our pyrodetectors, which see this background signal as a voltage offset. We took into account this offset in our comparison

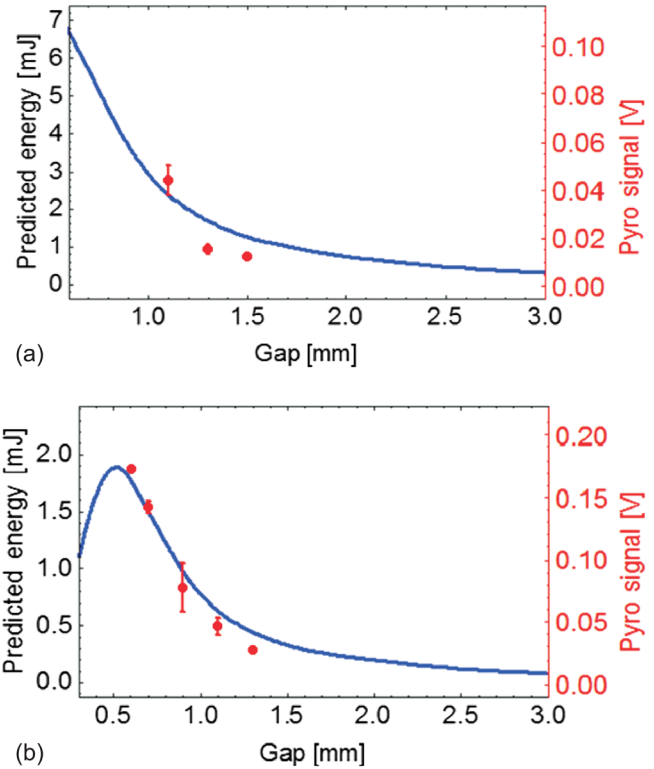


FIG. 16. Predicted (blue curve) and measured (red) peak pulse energy in a function of the gap, copper structure with a 3.2 nC electron beam (a) and copper-silver structure with a 1.6 nC electron beam (b).

between the measured pulse energy and the calculations shown in Figs. 15 and 16.

During a horizontal scan, we record the largest output energy when the beam is on the structure axis. Those measurements are shown in Fig. 16(a), as a function of the gap.

## 2. Measurement of electron beam deflection

During a horizontal scan, the beam is decelerated and horizontally deflected. We could clearly observe horizontal deflection of the beam centroid, from which the deflecting voltage was calculated using  $R_{12}$ . Figure 17 shows this analysis of a horizontal scan. Vertical error bars correspond to the standard deviation of the centroid positions caused by a transverse position jitter of the FACET bunch, pulse to pulse variation of the bunch shape, and rf breakdowns. We believe that the good correspondence between the simulated and measured deflecting voltages confirms our simulations of the accelerating voltage.

## 3. Measurement of breakdown rate in the copper structure

We measured the breakdown rate in two ways: with a constant gradient and at different gradients during a horizontal scan.

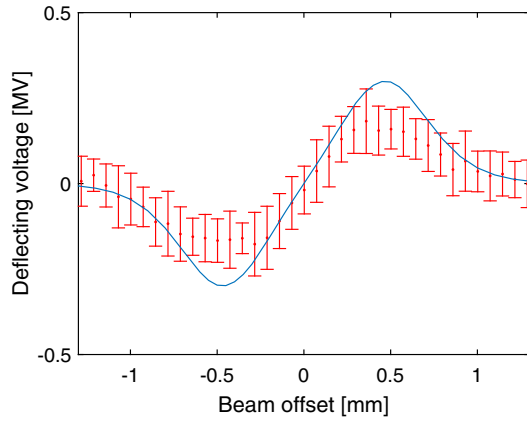


FIG. 17. Measurement of beam deflection in a horizontal scan with gap = 1.1 mm, a longitudinal bunch length  $\sigma_z$  of 50  $\mu\text{m}$ , and a charge of 3.2 nC (red plot). The blue plot is the simulation.

The constant gradient breakdown rate measurement was performed by positioning the beam on the central axis and by exposing the structure to a certain number of pulses (flat part of the pyrodetector signal in Fig. 14). At a fixed gap, we recorded the arc-detector data and then calculated the corresponding breakdown rate. Figure 18 shows how we detect breakdowns (copper structure with gap = 1.3 mm). Figure 18(a) shows the current monitor signal, where we set

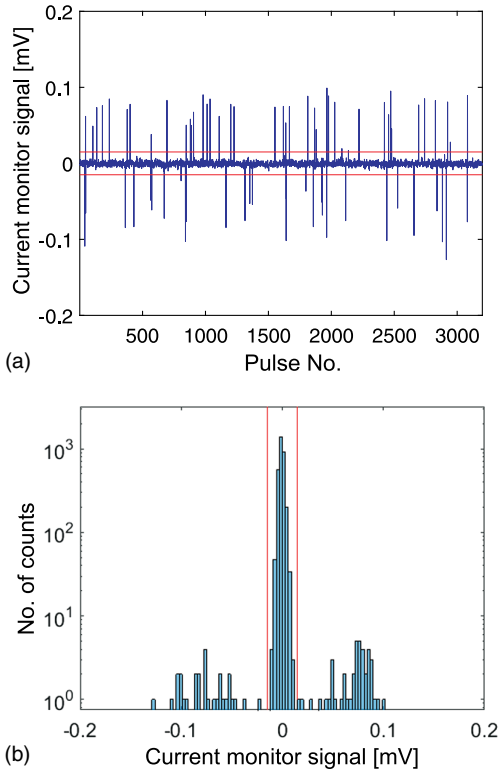


FIG. 18. Current monitor signal recorded by placing the electron beam in the central axis of the copper structure (a) and histogram of the distribution of the current monitor voltages (b), with 1.3 mm gap, 3.2 nC of bunch charge, and  $\sigma_z = 50 \mu\text{m}$ .

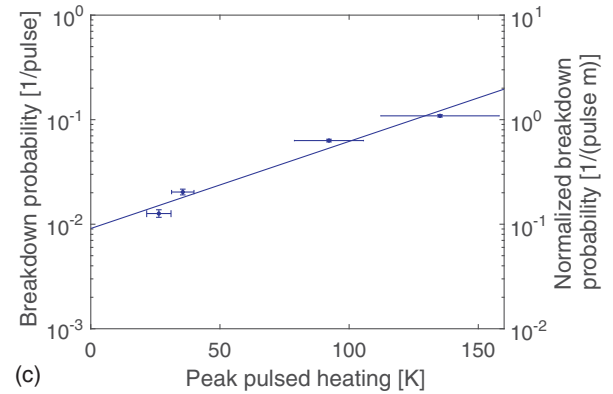
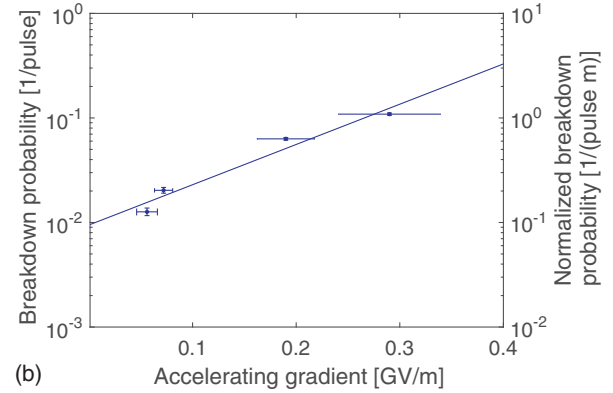
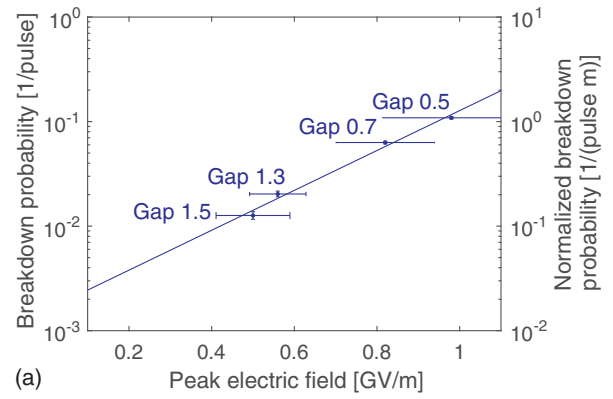


FIG. 19. Constant gradient breakdown rate measurements, obtained by placing the electron beam in the central axis of the copper structure, with 3.2 nC of bunch charge and  $\sigma_z = 50 \mu\text{m}$ , as a function of the peak electric field (a), as a function of the accelerating gradient (b), and as a function of the peak pulsed heating (c). The repetition rate varied from 1 to 15 Hz.

a threshold. The spikes with larger values than this threshold (in absolute value) are tagged as breakdowns. Figure 18(b) is the histogram of the distribution of the current monitor voltages. In the histogram representation, breakdowns are recognized when the histogram bars lie outside the red threshold lines. These breakdown rate measurements have been performed at different gaps. They are shown in Fig. 19, for the copper experiment

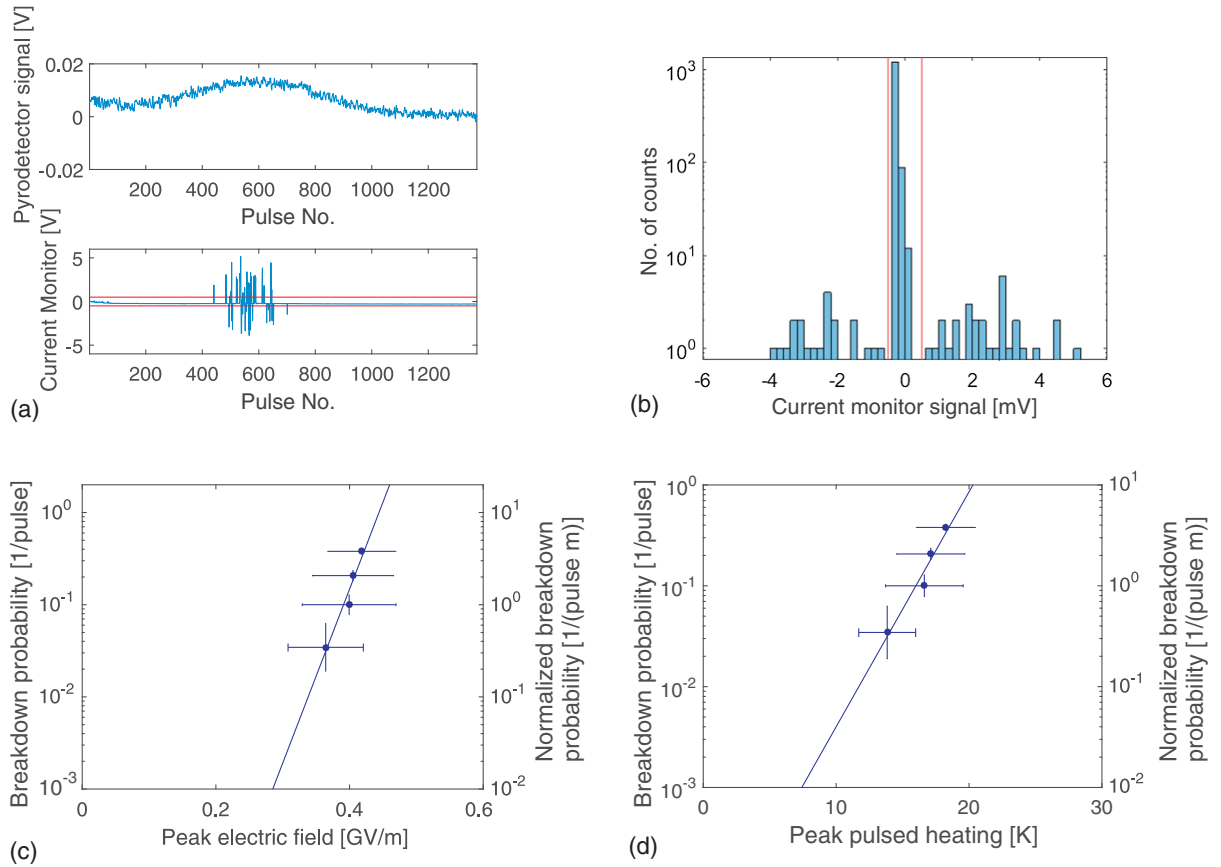


FIG. 20. Breakdown rate measurements, achieved during a horizontal scan of the copper structure with a 1.5 mm gap, with 3.2 nC of bunch charge and  $\sigma_z = 50 \mu\text{m}$ , plots of the pyrodetector signal and of the arc detector, showing that the arc probability increases with the gradient (a), the histogram of the distribution of the current monitor voltages (b), the breakdown rate as a function of the peak electric field (c), and as a function of the peak pulsed heating (d).

with 3.2 nC of bunch charge and  $\sigma_z = 50 \mu\text{m}$ . The repetition rate varied from 1 to 15 Hz. We normalized the breakdown rate per meter to compare it with our X-band experiments. We refer to Table III for the detailed correspondence between gaps and pulse lengths.

Another type of breakdown rate measurement was carried out during a horizontal scan where the scan starts clear of the corrugations. During the scan, the accelerating gradient first increases as the beam approaches the center axis and then decreases (see the bell-shaped curves of the pyrodetector signal in Fig. 14 and the loss factor simulations in Fig. 10). Per each discrete step of the horizontal scan, we recorded several arc-detector pulses and then calculated the corresponding breakdown rate. The results of this second type of breakdown rate measurements for the copper structure are shown in Fig. 20 with a 1.5 mm gap, 3.2 nC of bunch charge, and  $\sigma_z = 50 \mu\text{m}$ .

#### 4. Measurement of frequency with interferometer

Frequency measurements are made using a scanning Michelson interferometer [87]. A schematic of the device

is shown in Fig. 21. The incident rf signal is divided evenly using a splitter mounted  $45^\circ$  with respect to the beam [Fig. 21(a)]. One-half of the radiation is sent to a gold mirror mounted on a linear translation stage capable

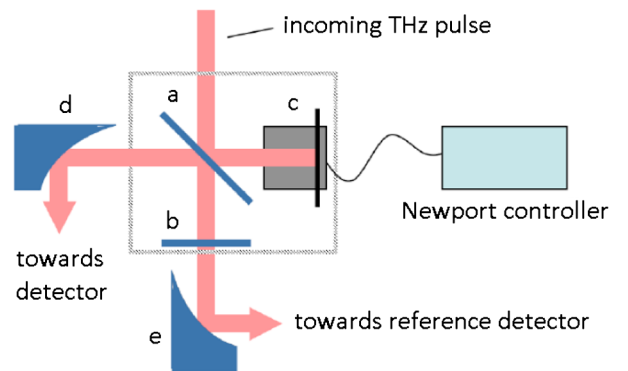


FIG. 21. Schematic of the interferometer, including the following components:  $45^\circ$  beam splitter (a),  $90^\circ$  beam splitter (b), front surface mirror on a translation stage (c), detector focusing mirror (d), and reference detector focusing mirror (e).

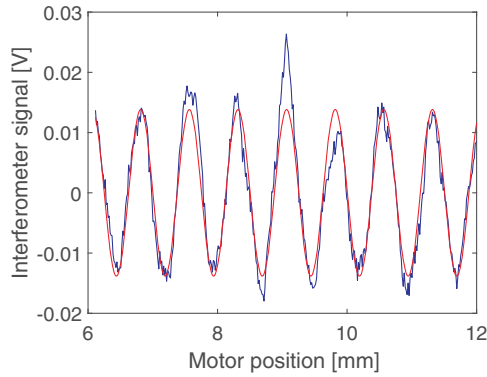


FIG. 22. Example of a frequency measurement carried out with the interferometer, where the blue curve is the interferometer pyrodetector signal as a function of the motor position, and the red curve is a sinusoidal fitting.

of 25.4 mm of travel [Fig. 21(c)]. The second half of the radiation is sent through another splitter, normal to the direction of propagation [Fig. 21(b)]. The rf signal transmitted through this second splitter is sent to a 3-inch off-axis parabolic (OAP) mirror of 6-inch focal length, focused onto a pyroelectric detector, and used as a reference signal to control for variations of incident intensity [Fig. 21(e)]. The rf power reflected from the second splitter is recombined with the rf reflected from the gold mirror and sent to another 3-inch 90° OAP,

of 3-inch focal length, which focuses the interfering radiation on a pyro identical to the reference pyro [Fig. 21(d)].

The linear translation stage allows the interfering signals to be delayed with respect to one another by 50.8 mm, resulting in a theoretical frequency resolution of 5.9 GHz. This resolution was benchmarked using broadband radiation generated by the beam to measure the three water lines in air and found to be in excellent agreement with the theory and other experimental measurements. The stage’s minimum step size of 0.5  $\mu\text{m}$  results in a maximum measurable frequency of 150 THz.

An example of a single frequency measurement carried out with the interferometer is shown in Fig. 22. The blue curve is the interferometer pyrodetector signal as a function of the interferometer motor position, and the red curve is a sinusoidal fitting. The frequency of the emitted radiation is obtained from the fitting parameter.

The results of the frequency measurements as a function of the gap are shown in Fig. 5(a). We have good agreement between the calculations (blue plot) and measurements (red plot).

### 5. Scanning electron microscope inspection of the copper structure

After the experiment, we inspected the structure surfaces with a SEM microscope. The results of the

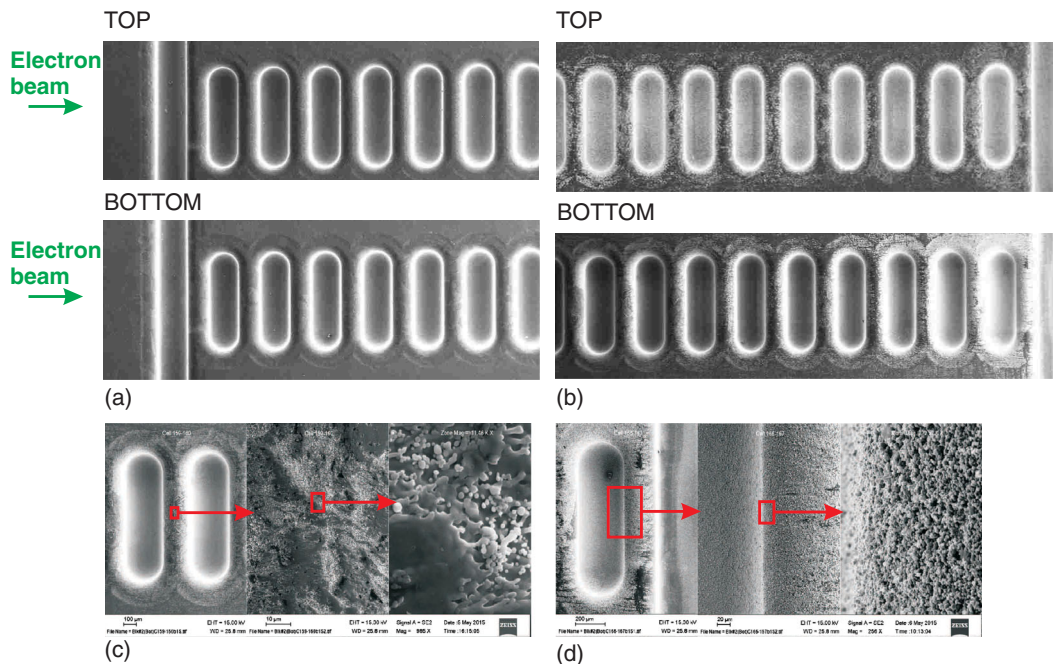


FIG. 23. SEM picture of breakdowns generated during the experiment involving the 235 GHz copper structure, driven by a bunch charge of 3.2 nC and 50  $\mu\text{m}$  length. Input part of the structure: Little damage sign, from the input coupler to cell 152 (a). Output end of the structure: Damage concentrated at output irises, the bottom part has more sputter, and all the heavy damage occurs in cells 154–167 (b); iris between cells 159 and 160, heavy damage (c); bottom cell 166, areas adjacent to heavy surface melting are covered with sputtered material (d).

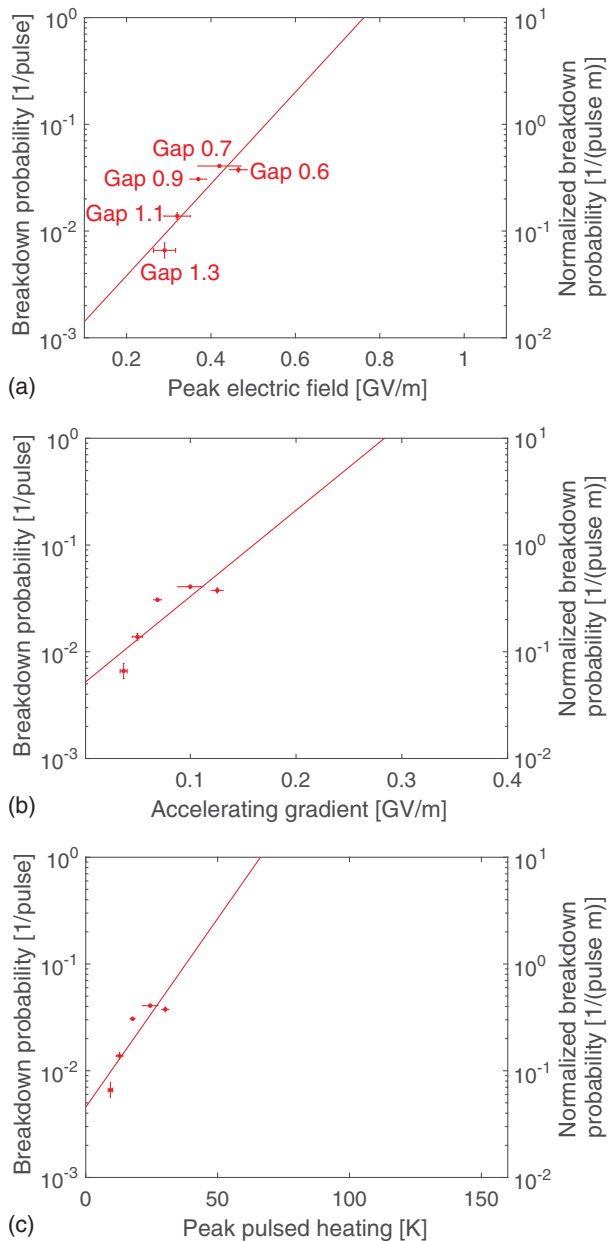


FIG. 24. Constant gradient breakdown rate measurements, obtained by placing the electron beam in the central axis of the copper-silver structure, with 1.6 nC of bunch charge and  $\sigma_z = 25 \mu\text{m}$ , as a function of the peak electric field (a), as a function of the accelerating gradient (b), and as a function of the peak pulsed heating (c). The repetition rate was 29 Hz.

SEM are shown in Fig. 23. The input part of the structure shows little damage, from the input coupler to cell 152. The output end of the structure shows damage concentrated at output irises, the bottom part showing more sputter, and all the heavy damage occurs in cells 154–167. The iris between cells 159 and 160 suffered heavy damage, and in the bottom cell 166 the areas adjacent to heavy surface melting

are covered with sputtered material. We conjecture that these damages are consistent with damage due to rf breakdowns, because in the output part of the structure the rf pulse length excited by the beam is the largest.

### E. Experimental results with the 235 GHz traveling-wave copper-silver structure

In the experiment involving the copper-silver structure (May 15, 2015), the bunch charge was 1.6 nC,  $\sigma_z = 25 \mu\text{m}$ , and the repetition rate was 29 Hz. We performed several horizontal scans and frequency measurements with interferometers and measured breakdown rate statistics. The gap varied from 1.3 to 0.5 mm.

During a horizontal scan, we record the largest output energy when the beam is on the structure axis. Those measurements are shown in Fig. 16(b), as a function of the gap.

#### 1. Measurement of breakdown rate in the copper-silver structure

In the copper-silver structure, we measured the constant gradient breakdown statistics by positioning the beam on the central axis and by exposing the structure to a certain number of pulses (flat part of the pyrodetector signal in Fig. 14). At a fixed gap, we recorded the arc-detector data and then calculated the corresponding breakdown rate. The results are shown in Fig. 24 with 1.6 nC of bunch charge and  $\sigma_z = 25 \mu\text{m}$ . The repetition rate of this experiment was 29 Hz, which gives higher breakdown rates with respect to the copper case (where the repetition rate varied from 1 to 15 Hz). At a higher repetition rate, there are a series of events that can contribute to higher breakdown rate, such as increased vacuum outgassing, increased exposure to radiation, and a larger quantity of beam halo electrons intercepted by the structure. We refer to Table III for the detailed correspondence between gaps and pulse lengths.

#### 2. Scanning electron microscope inspection of the copper-silver structure

After the experiment, we inspected the structure surfaces with a SEM microscope. The results of the SEM are shown in Fig. 25. The input part of the structure shows little damage, from the input coupler to cell 149. The output end of the structure shows areas of heavy damage and surface melting occurring after cell 155. The iris between cells 155 and 156 suffers damage and surface melting. We conjecture that these damages are consistent with damage due to rf breakdowns.

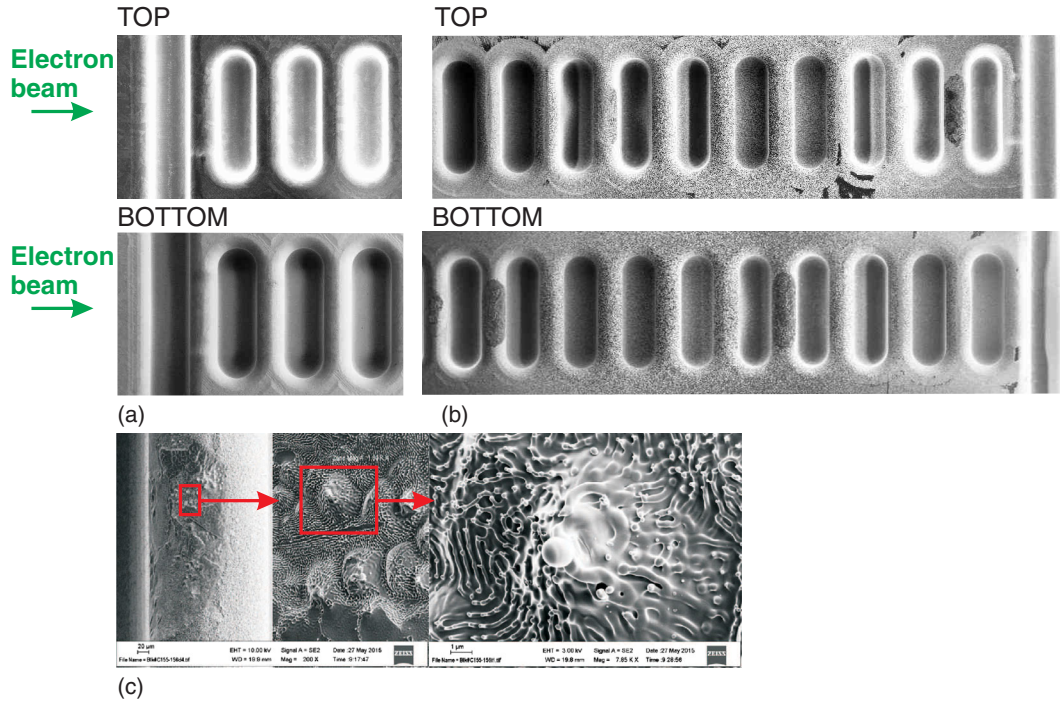


FIG. 25. SEM picture of breakdowns generated during the experiment involving the 235 GHz copper-silver structure, driven by a bunch charge of 1.6 nC and 25  $\mu\text{m}$  length. Input part of the structure: Little damage sign, from the input coupler to cell 149 (a). Output end of the structure: First areas of heavy arcing and surface melting occur after cell 155 (b); iris between cells 155 and 156, damage and surface melting (c).

## V. DISCUSSION

We conjecture that the behavior of the arc-detector spikes is consistent with the behavior of rf breakdowns: the breakdown rate increases with increased rf fields, and it increases with increased pulsed surface heating (see Figs. 19 and 24). In addition, the current pulses measured with the arc detector have both positive and negative polarities, consistent with rf breakdowns generated on the top and bottom of the structure, and the damage observed with the SEM is in the output part of the structure, where the rf pulse length is the longest and thus the pulsed heating is higher. We conjecture that these damages are consistent with damage due to rf breakdowns.

During the NLC/GLC work, the statistical nature of rf breakdown in 11 GHz (*X*-band) accelerating structures became apparent [2,3,12,24,88]. In the experiments reported in this paper, we observed that also the rf breakdowns on 200 GHz structures have a similar statistical behavior, which allows the quantitative measurement of the breakdown probability.

The main difference between 11 and 200 GHz results is that at these higher frequencies we observed a possible dependence of the breakdown rate on the repetition rate.

The measured breakdown rates are relatively high for the field levels and pulse lengths as compared to values extrapolated from *X*-band experiments [9,24]. Typically, *X*-band accelerating structures were conditioned by more than  $10^8$  rf

pulses, without beam and vacuum pressures below  $10^{-8}$  Torr. In this experiment, the rf field is excited by the FACET beam, so the number of pulses was limited to  $< 10^6$  by the practical length of the experimental shift, and the vacuum level is about  $10^{-6}$  Torr. We conjecture that the breakdown rate is expected to improve with a better vacuum and more conditioning time. The presence of the FACET beam could have increased the breakdown rate. The beam halo was intercepted by the structure, and, a few times, the whole beam was dumped into the structure due to linac faults.

In our *X*-band experiments, copper-silver accelerating structures typically have a lower breakdown rate than copper structures. In the experiments presented in this paper, the breakdown rate was higher in the copper-silver structure. To obtain a measurable breakdown rate, we kept the breakdown rate below saturated one breakdown per rf pulse (where a rf pulse is generated by a FACET electron beam shot). To improve the statistics we varied the beam repetition rate to accumulate more pulses. During the experiment with the copper structure, FACET provided a beam repetition rate that varied from 1 to 15 Hz, and the repetition rate was 29 Hz in the experiment with the copper-silver structure. Comparing Figs. 19 and 24, copper-silver has a higher breakdown rate for the same gradient and pulsed surface heating. This result is inconsistent with the ones obtained for the *X*-band copper-silver structures. We speculate that with the copper-silver structure the higher beam repetition rate could have increased the breakdown

rate. Possible explanations are the increased vacuum pressure or increase of an adverse effect of the FACET beam with the increased repetition rate.

## VI. CONCLUSIONS

We report the first experimental measurements of rf breakdown statistics, frequency, and deflecting forces in a copper and copper-silver traveling-wave accelerating structure at 200 GHz frequencies.

Deflecting voltage was measured by observing the displacement of the electron beam on a diagnostic screen downstream of the structure. This measurement confirms our simulated values of deflecting and accelerating gradients.

We measure the breakdown rate statistics at different gap sizes between the two structure halves, different beam position vs the central axis, and different pulse repetition rates.

The breakdown rate of the copper structure was  $10^{-2}$  per pulse [which normalized to  $L = 10$  cm is  $0.1/(\text{pulse m})$ ], with a peak surface electric field of 500 MV/m, which for a relatively large beam aperture  $a/\lambda = 0.5$  corresponds to an accelerating gradient of 56 MV/m, at a rf pulse length of 0.3 ns, and a peak pulsed surface heating of 26 K (as shown in Fig. 19), with a repetition rate as high as 15 Hz. For the same breakdown rate, the copper-silver structure had a peak electric field of 320 MV/m, which for  $a/\lambda = 0.37$  corresponds to an accelerating gradient of 50 MV/m, at a pulse length of 0.5 ns, and a peak pulsed surface heating of 12 K (as shown in Fig. 24), with a 29 Hz repetition rate.

We conjecture that the presence of the FACET beam and the limited number of conditioning pulses both could have increased the breakdown rate. We are working on future experiments where high-gradient accelerating cavities will be powered by rf sources in order to avoid the influence of the driving beam on the rf breakdown performance.

These studies will pave the way towards the use of subterahertz devices in future accelerator applications.

## ACKNOWLEDGMENTS

This work was supported by the U.S. Department of Energy under Contract No. DE-AC02-76SF00515. We thank all the E204 experiment crew: Juan Cruz, Jr.; rf diagnostics, Spencer Gessner, Oliver Williams (UCLA), and Filippou Toufexis; SEM, Chris Pearson; and machine optics and other information, Erik Adli, Carl Andreas Lindstrom, and Michael Litos. We thank Vitaly Yakimenko and the FACET team for excellent support. We thank Warner Bruns for his support with the GADFL calculation software.

[1] R. B. Neal, D. W. Dupen, H. A. Hogg, and G. A. Loew, Stanford University Report No. SLAC-REPRINT-1968-001, 1968.

- [2] S. Doebert *et al.*, High gradient performance of NLC/GLC X-band accelerating structures, in *Proceedings of the 21st Particle Accelerator Conference, Knoxville, TN, 2005* (IEEE, Piscataway, NJ, 2005), pp. 372–374 (Report No. SLAC-PUB-11207).
- [3] J. W. Wang, R&D of accelerator structures at SLAC, High Energy Phys. Nucl. Phys. **30**, 11 (2006).
- [4] G. Guignard, CERN Report No. CERN 2000-008, 2000.
- [5] F. V. Hartemann and F. Albert, LLNL Technical Report No. LLNL-TR-416320, 2009.
- [6] D. H. Whittum, Millimeter-Wave Drivers for Future Linear Colliders, in *Proceedings of the 22nd International Conference on Infrared and Millimeter Waves, Wintergreen, 1998* (Report No. SLAC-PUB-7809, 1998).
- [7] V. E. Balakin, O. N. Brezhnev, A. V. Novokhatsky, and Yu. I. Semenov, Report No. SLAC-TRANS-0187, 1978.
- [8] G. A. Loew and J. W. Wang, Report No. SLAC-PUB-4647, 1988.
- [9] H. H. Braun, S. Döbert, I. Wilson, and W. Wuensch, Frequency and Temperature Dependence of Electrical Breakdown at 21, 30, and 39 GHz, *Phys. Rev. Lett.* **90**, 224801 (2003).
- [10] D. Yu, H. Henke, H. H. Braun, S. Dobert, and W. Wuensch, High power test of a 30-GHz planar accelerator, in *Proceedings of the 19th Particle Accelerator Conference, Chicago, IL, 2001* (IEEE, Piscataway, NJ, 2001), Vol. 5, pp. 3858–3860.
- [11] W. W. H. Braun and M. Valentini, Report No. CERN-CLIC-NOTE-413, 1999.
- [12] C. Adolphsen, Normal Conducting rf Structure Test Facilities and Results, in *Proceedings of the 2003 Particle Accelerator Conference, Portland, OR* (IEEE, New York, 2003), pp. 668–672.
- [13] G. Geschonke, Result from the CLIC Test Facility CTF3 and Update on the CLIC Design, in *Proceedings of the 11th European Particle Accelerator Conference, Genoa, 2008* (EPS-AG, Genoa, Italy, 2008), pp. 2912–2916.
- [14] G. D’Auria, X-band technology applications at FERMI@Elettra FEL project, *Nucl. Instrum. Methods Phys. Res., Sect. A* **657**, 150 (2011).
- [15] J. Beijers *et al.*, ZFEL: A Compact, Soft X-ray FEL in the Netherlands, in *Proceedings of the 32nd Free Electron Laser Conference, Malmö, Sweden* (Max-lab, Sweden, 2010), pp. 163–164.
- [16] U. Amaldi *et al.*, Cyclinacs: Fast-cycling accelerators for hadron therapy, [arXiv:0902.3533](https://arxiv.org/abs/0902.3533).
- [17] A. E. Vliet *et al.*, Initial Testing of the Mark-0 X-Band RF Gun at SLAC, in *Proceedings of the 3rd International Particle Accelerator Conference, New Orleans, LA, 2012* (IEEE, Piscataway, NJ, 2012).
- [18] P. McIntosh *et al.*, Realization of an X-Band RF System for LCLS, in *Proceedings of the 21st Particle Accelerator Conference, Knoxville, TN, 2005* (IEEE, Piscataway, NJ, 2005).
- [19] V. A. Dolgashev, X-Band Deflectors, in *Proceedings of the ICFE Beam Dynamics Mini-Workshop on Deflecting/Crabbing Cavity Applications in Accelerators, Cockcroft Institute, 2010* (CERN, Daresbury, 2010).
- [20] V. A. Dolgashev, G. Bowden, Y. Ding, P. Emma, P. Krejcik, J. Lewandowski, C. Limborg, M. Litos, J. Wang, and D. Xiang, Design and application of multimewatt X-band

- deflectors for femtosecond electron beam diagnostics, *Phys. Rev. ST Accel. Beams* **17**, 102801 (2014).
- [21] P. Craievich, M. Petronio, S. G. Biedron, D. Castronovo, M. D. Forno, S. D. Mitri, N. Faure, D. L. Civita, G. Penco, L. Rumiz, L. Sturari, R. Vescovo, and D. Wang, Implementation of radio-frequency deflecting devices for comprehensive high-energy electron beam diagnosis, *IEEE Trans. Nucl. Sci.* **62**, 210 (2015).
- [22] S. G. Tantawi *et al.*, Application of the Balanced Hybrid Mode in Overmoded Corrugated Waveguides to Short Wavelength Dynamic Undulators, in *Proceedings of the 2nd International Particle Accelerator Conference, San Sebastián, Spain* (EPS-AG, Spain, 2011).
- [23] S. Tantawi, M. Shumail, J. Neilson, G. Bowden, C. Chang, E. Hemsing, and M. Dunning, Experimental Demonstration of a Tunable Microwave Undulator, *Phys. Rev. Lett.* **112**, 164802 (2014).
- [24] V. A. Dolgashev, Progress on high-gradient structures, *AIP Conf. Proc.* **1507**, 76 (2012).
- [25] J. Wang *et al.*, Fabrication Technologies of the High Gradient Accelerator Structures at 100 MV/m Range, in *Proceedings of the International Particle Accelerator Conference, Kyoto, Japan* (ICR, Kyoto, 2010).
- [26] T. Higo *et al.*, Advances in X-band TW Accelerator Structures Operating in the 100 MV/m Regime, in *Proceedings of the International Particle Accelerator Conference, Kyoto, Japan* (ICR, Kyoto, 2010), pp. 3702–3704.
- [27] T. Higo, Progress of X-band Accelerating Structures, in *Proceedings of the 25th International Linear Accelerator Conference, LINAC-2010, Tsukuba, Japan* (KEK, Tsukuba, Japan, 2010).
- [28] International Workshop on Breakdown Science and High Gradient Accelerator Technology (HG2016), *Proceedings of the International Workshop on Breakdown Science and High Gradient Accelerator Technology (HG2016)* (Argonne National Laboratory, Lemont, 2016), <https://indico.hep.anl.gov/indico/conferenceDisplay.py?confId=963>.
- [29] N. Catalan, CERN Testing Program: Plans and Schedule, in *Proceedings of the International Workshop on Breakdown Science and High Gradient Accelerator Technology (HG2016)* (Argonne National Laboratory, Lemont, 2016).
- [30] W. Wuensch, Status and objectives of the CLIC X-band activity, in *Proceedings of the International Workshop on Breakdown Science and High Gradient Technology, Tsukuba, Japan, 2012* (CERN, Tsukuba, 2012).
- [31] V. Dolgashev, High gradient results from single-cell setup, in *Proceedings of the International Workshop on Breakdown Science and High Gradient Technology, Tsukuba, Japan, 2012* (CERN, Tsukuba, 2012).
- [32] V. Dolgashev, S. Tantawi, Y. Higashi, and B. Spataro, Geometric dependence of radio-frequency breakdown in normal conducting accelerating structures, *Appl. Phys. Lett.* **97**, 171501 (2010).
- [33] F. Wang, C. Adolphsen, and C. Nantista, Performance limiting effects in X-band accelerators, *Phys. Rev. ST Accel. Beams* **14**, 010401 (2011).
- [34] V. A. Dolgashev and S. G. Tantawi, Simulations of Currents in X-band accelerator structures using 2D and 3D particle-in-cell code, in *Proceedings of the 19th Particle Accelerator Conference, Chicago, IL, 2001* (IEEE, Piscataway, 2001), pp. 3807–3809.
- [35] V. Dolgashev and S. Tantawi, Effect of RF parameters on breakdown limits in high-vacuum X-band structures, *AIP Conf. Proc.* **691**, 151 (2003).
- [36] V. A. Dolgashev, High magnetic fields in couplers of X-band accelerating structures, in *Proceedings of the 2003 Particle Accelerator Conference, Portland, OR* (IEEE, New York, 2003), pp. 1267–1269 (Report No. SLAC-PUB-10123).
- [37] V. A. Dolgashev and S. G. Tantawi, RF Breakdown in X-band Waveguides, in *Proceedings of the 8th European Particle Accelerator Conference, Paris, 2002* (EPS-IGA and CERN, Geneva, 2002), pp. 2139–2141.
- [38] A. Grudiev, S. Calatroni, and W. Wuensch, New local field quantity describing the high gradient limit of accelerating structures, *Phys. Rev. ST Accel. Beams* **12**, 102001 (2009).
- [39] D. Whittum, H. Henke, and P. Chou, High-gradient cavity beat-wave accelerator at W-band, in *Proceedings of the Particle Accelerator Conference, Vancouver, BC, 1997* (IEEE, New York, 1997), Vol. 1, pp. 542–544.
- [40] A. W. Chao and M. Tigner, *Handbook of Accelerator Physics and Engineering* (World Scientific, Singapore, 1999).
- [41] D. H. Whittum and S. G. Tantawi, Switched matrix accelerator, *Rev. Sci. Instrum.* **72**, 73 (2001).
- [42] D. H. Whittum and S. G. Tantawi, Report No. SLAC-PUB 7845, 1998.
- [43] SLAC W-band program, <http://www.slac.stanford.edu/grp/arb/tn/histpap/wband/>.
- [44] D. Yu, S. Ben-Menahem, P. Wilson, R. Miller, R. Ruth, and A. Nassiri, High frequency planar accelerating structures for future linear colliders, *AIP Conf. Proc.* **335**, 800 (1995).
- [45] M. E. Hill, C. Adolphsen, W. Baumgartner, R. S. Callin, X. E. Lin, M. Seidel, T. Slaton, and D. H. Whittum, High-Gradient Millimeter-Wave Accelerator on a Planar Dielectric Substrate, *Phys. Rev. Lett.* **87**, 094801 (2001).
- [46] M. Hill, W. Fowkes, X. Lin, and D. Whittum, Beam-cavity interaction circuit at W-band, *IEEE Trans. Microwave Theory Tech.* **49**, 998 (2001).
- [47] M. Hill, R. Callin, M. Seidel, and D. Whittum, High-power squeeze-type phase shifter at W-band, *IEEE Trans. Microwave Theory Tech.* **50**, 1437 (2002).
- [48] M. Hill, R. Callin, and D. H. Whittum, High-power vacuum window in WR10, *IEEE Trans. Microwave Theory Tech.* **49**, 994 (2001).
- [49] F. Zimmermann, D. H. Whittum, C. K. Ng, and M. E. Hill, Wake fields in a mm-wave linac, *AIP Conf. Proc.* **472**, 270 (1999).
- [50] H. Henke, Planar structures for electron acceleration, in *Proceedings of the Particle Accelerator Conference, Dallas, TX, 1995* (IEEE, New York, 1995), Vol. 3, pp. 1750–1752.
- [51] B. Littmann and H. Henke, Feasibility study of optically coupling RF-power at mm waves, in *Proceedings of the Particle Accelerator Conference, Dallas, TX, 1995* (IEEE, New York, 1995), Vol. 3, pp. 1593–1595.
- [52] W. Bruns, Design of input couplers and endcells for side coupled muffin-tin structures, in *Proceedings of the*

- Particle Accelerator Conference, Dallas, TX, 1995* (IEEE, New York, 1995), Vol. 2, pp. 1088–1089.
- [53] W. Bruns, Error sensitivity study for side coupled muffin tin structures using a finite difference program, in *Proceedings of the Particle Accelerator Conference, Dallas, TX, 1995* (IEEE, New York, 1995), Vol. 2, pp. 1085–1087.
- [54] P. Chou, G. Bowden, M. Copeland, H. Henke, A. Menegat, and R. Siemann, Design and fabrication of a traveling-wave muffin-tin accelerating structure at 90 GHz, in *Proceedings of the Particle Accelerator Conference, Vancouver, BC, Canada, 1997* (IEEE, New York, 1997), Vol. 1, pp. 464–466.
- [55] P. J. Chou, G. B. Bowden, M. R. Copeland, A. Farvid, R. E. Kirby, A. Menegat, C. Pearson, L. Shere, R. H. Siemann, J. E. Spencer, and D. H. Whittum, The fabrication of millimeter-wavelength accelerating structures, *AIP Conf. Proc.* **398**, 501 (1997).
- [56] P. Chou, G. Bowden, M. Copeland, H. Henke, A. Menegat, D. Pritzkau, and R. Siemann, RF measurements of a traveling wave muffin-tin accelerating structure at 90 GHz, in *Proceedings of the Particle Accelerator Conference, Vancouver, BC, Canada, 1997* (IEEE, New York, 1997), Vol. 1, pp. 672–674.
- [57] N. Kroll, E. Hill, X. Lin, R. Siemann, D. Vier, D. Whittum, and D. Palmer, Planar accelerator structures for millimeter wavelengths, in *Proceedings of the 18th Particle Accelerator Conference, New York, 1999* (IEEE, New York, 1999), Vol. 5, pp. 3612–3614.
- [58] Facility for advanced accelerator experimental tests Facility for advanced accelerator experimental tests (FACET), <http://facet.slac.stanford.edu/>.
- [59] B. D. O’Shea, G. Andonian, S. K. Barber, K. L. Fitzmorris, S. Hakimi, J. Harrison, P. D. Hoang, M. J. Hogan, B. Naranjo, O. B. Williams, V. Yakimenko, and J. B. Rosenzweig, Observation of acceleration and deceleration in gigaelectron-volt-per-metre gradient dielectric wakefield accelerators, *Nat. Commun.* **7**, 12763 (2016).
- [60] G. Andonian, D. Stratakis, M. Babzien, S. Barber, M. Fedurin, E. Hemsing, K. Kusche, P. Muggli, B. O’Shea, X. Wei, O. Williams, V. Yakimenko, and J. B. Rosenzweig, Dielectric Wakefield Acceleration of a Relativistic Electron Beam in a Slab-Symmetric Dielectric Lined Waveguide, *Phys. Rev. Lett.* **108**, 244801 (2012).
- [61] M. C. Thompson *et al.*, Ultra-High Gradient Dielectric Wakefield Accelerator Experiments, <http://www.osti.gov/scitech/servlets/purl/894768>.
- [62] M. C. Thompson, H. Badakov, A. M. Cook, J. B. Rosenzweig, R. Tikhoplav, G. Travish, I. Blumenfeld, M. J. Hogan, R. Ischebeck, N. Kirby, R. Siemann, D. Walz, P. Muggli, A. Scott, and R. B. Yoder, Breakdown Limits on Gigavolt-per-Meter Electron-Beam-Driven Wakefields in Dielectric Structures, *Phys. Rev. Lett.* **100**, 214801 (2008).
- [63] J. B. Rosenzweig, G. Andonian, P. Muggli, P. Niknejadi, G. Travish, O. Williams, K. Xuan, and V. Yakimenko, High frequency, high gradient dielectric wakefield acceleration experiments at SLAC and BNL, *AIP Conf. Proc.* **1299**, 364 (2010).
- [64] D. Wang, S. Antipov, C. Jing, J. G. Power, M. Conde, E. Wisniewski, W. Liu, J. Qiu, G. Ha, V. Dolgashev, C. Tang, and W. Gai, Interaction of an Ultrarelativistic Electron Bunch Train with a W-Band Accelerating Structure: High Power and High Gradient, *Phys. Rev. Lett.* **116**, 054801 (2016).
- [65] W. Gai, P. Schoessow, B. Cole, R. Konecny, J. Norem, J. Rosenzweig, and J. Simpson, Experimental Demonstration of Wake-Field Effects in Dielectric Structures, *Phys. Rev. Lett.* **61**, 2756 (1988).
- [66] M. Conde, S. Antipov, W. Gai, C. Jing, R. Konecny, W. Liu, J. Power, H. Wang, and Z. Yusof, The Argonne Wakefield Accelerator Facility: Status and Recent Activities, in *Proceedings of the 21st Particle Accelerator Conference, Knoxville, TN, 2005* (IEEE, Piscataway, NJ, 2005), pp. 1485–1487.
- [67] M. Conde, Survey of advanced dielectric wakefield accelerators, in *Proceedings of the 22nd Particle Accelerator Conference, PAC-2007, Albuquerque, NM* (IEEE, New York, 2007), pp. 1899–1903.
- [68] M. Dal Forno, V. Dolgashev, G. Bowden, C. Clarke, M. Hogan, D. McCormick, A. Novokhatski, B. Spataro, S. Weathersby, and S. G. Tantawi, rf breakdown tests of mm-wave metallic accelerating structures, *Phys. Rev. Accel. Beams* **19**, 011301 (2016).
- [69] M. Dal Forno, V. Dolgashev, G. Bowden, C. Clarke, M. Hogan, D. McCormick, A. Novokhatski, B. Spataro, S. Weathersby, and S. G. Tantawi, Experimental measurements of rf breakdowns and deflecting gradients in mm-wave metallic accelerating structures, *Phys. Rev. Accel. Beams* **19**, 051302 (2016).
- [70] High frequency structural simulator High frequency structural simulator (HFSS), <http://www.ansys.com/Products/>.
- [71] A. Smirnov, Group velocity effect on resonant, long-range wake-fields in slow wave structures, *Nucl. Instrum. Methods Phys. Res., Sect. A* **480**, 387 (2002).
- [72] K. L. F. Bane and G. Stupakov, Impedance of a rectangular beam tube with small corrugations, *Phys. Rev. ST Accel. Beams* **6**, 024401 (2003).
- [73] A. Millich and L. Thorndahl, Report No. CERN-CLIC-NOTE-366, 1999.
- [74] C. Nantista, S. Tantawi, and V. A. Dolgashev, Low-field accelerator structure couplers and design techniques, *Phys. Rev. ST Accel. Beams* **7**, 072001 (2004).
- [75] M. Dal Forno, P. Craievich, G. Penco, and R. Vescovo, Theoretical and experimental analysis of a linear accelerator endowed with single feed coupler with movable short-circuit, *Rev. Sci. Instrum.* **84**, 114701 (2013).
- [76] P. B. Wilson, Scaling linear colliders to 5 TeV and above, *AIP Conf. Proc.* **397**, 191 (1997).
- [77] L. Laurent, S. Tantawi, V. Dolgashev, C. Nantista, Y. Higashi, M. Aicheler, S. Heikkinen, and W. Wuensch, Experimental study of rf pulsed heating, *Phys. Rev. ST Accel. Beams* **14**, 041001 (2011).
- [78] D. P. Pritzkau and R. H. Siemann, Experimental study of rf pulsed heating on oxygen free electronic copper, *Phys. Rev. ST Accel. Beams* **5**, 112002 (2002).
- [79] V. Dolgashev, S. Tantawi, Y. Higashi, and T. Higo, Status of High Power Tests of Normal Conducting Single-cell Structures, in *Proceedings of the 11th European Particle Accelerator Conference, Genoa, 2008* (EPS-AG, Genoa, Italy, 2008), pp. 742–744.

- 
- [80] CST (Darmstadt, Germany), <http://www.cst.de/>.
- [81] GdfidL (Germany), <http://www.gdfidl.de/>.
- [82] A. Novokhatsky, Report No. SLAC-PUB-11556, 2005.
- [83] A. Novokhatski, Field dynamics of coherent synchrotron radiation using a direct numerical solution of Maxwell's equations, *Phys. Rev. ST Accel. Beams* **14**, 060707 (2011).
- [84] A. Novokhatsky, Report No. SLAC-PUB-15258, 2012.
- [85] V. Balakin, I. Koop, A. Novokhatski, A. S. Skrinski, and V. Smirnov, Report No. SLAC-TRANS-0188, 1978.
- [86] EDM Department Inc. (Bartlett, IL), <http://www.edmdept.com/>.
- [87] A. A. Michelson and E. W. Morley, On the relative motion of the Earth and of the luminiferous ether, *Sidereal Messenger* **6**, 306 (1887).
- [88] A. Korsback, Statistics of breakdown and conditioning in pulsed dc and rf systems, in *Proceeding of the Mini MeVArc meeting (mini-MeVArc), 2016* (CERN, Geneva, 2016).